

Parameter Estimation of Global 21cm Signal

Aryana Haghjoo



Department of Physics
McGill University
Trottier Space Institute
Montréal, Québec, Canada

August 2023

A thesis submitted to McGill University in partial fulfillment of the requirements of the degree of

Master's of Science in Physics

©2023 Author

Abstract

The global 21cm signal has emerged as a crucial observable in cosmology and astrophysics, providing valuable insights in the study of the period between the end of the cosmic dark ages and the formation of the first stars and galaxies.

The 21cm signal is sensitive to the density and temperature of neutral hydrogen in the early universe and the presence of the first stars and galaxies. Therefore, any deviation from the predictions of the standard cosmological model of this signal could indicate the presence of new physics beyond the standard model. In this study, we explore the potential of this signal to reveal non-standard physics by means of providing a new path to test fundamental physical theories.

The literature review of this thesis provides a comprehensive overview by exploring the physical principles, simulations, imprints of non-standard effects, and observation attempts of the global 21cm signal. The physical principles encompass the mechanisms forming the global 21cm signal and its evolution through cosmic history. Simulations play a pivotal role in generating models of the global 21cm signal, aiding in understanding the influence of

different astrophysical scenarios on the ultimate behavior of this signal. Furthermore, the effects of non-standard physics on the global 21cm signal are examined, including scenarios such as cosmic strings, exotic particle interactions, or additional dark matter components. The review also explores ongoing efforts and challenges in observing the global 21cm signal and the complexities of foreground removal.

Furthermore, parameter estimation techniques are discussed, highlighting the methodologies employed to extract valuable astrophysical information from the observed 21cm data. Ultimately, this thesis focuses on a specific parameter estimation method, which adopts the combinations of Markov Chain Monte Carlo (MCMC) with the Levenberg Marquardt (LM) algorithm to estimate the best-fit physical parameters of the 21cm curves. Accelerated Reionization Era Simulations (ARES) is employed to generate theoretical models of the global 21cm signal. This method provides comprehensive control over the parameters of the algorithm, allowing to opt for any combination of parameters available within the ARES framework.

The knowledge of these best-fit parameters is expected to assist in constraining future proposed models and set theoretical limits for the precision of upcoming experiments to observe desired non-standard effects.

Résumé

Le signal global 21cm est devenu une observable cruciale en cosmologie et en astrophysique, fournissant des informations précieuses pour l'étude de la période entre la fin des âges sombres cosmiques et la formation des premières étoiles et galaxies.

Le signal 21cm est sensible à la densité et à la température de l'hydrogène neutre dans l'univers primitif et à la présence des premières étoiles et galaxies. Par conséquent, toute déviation de ce signal par rapport aux prédictions du modèle cosmologique standard pourrait indiquer la présence d'une nouvelle physique au-delà du modèle standard. Dans cette étude, nous explorons le potentiel de ce signal à révéler une physique non standard en fournissant une nouvelle voie pour tester les théories physiques fondamentales.

La revue de la littérature de cette thèse fournit une vue d'ensemble complète en explorant les principes physiques, les simulations, les empreintes d'effets non-standard, et les tentatives d'observation du signal global 21cm . Les principes physiques englobent les mécanismes qui forment le signal global 21cm et son évolution au cours de l'histoire cosmique. Les simulations jouent un rôle essentiel dans la génération de modèles du signal global 21cm ,

aidant à comprendre l'influence de différents scénarios astrophysiques sur le comportement final de ce signal. En outre, les effets de la physique non standard sur le signal global $21cm$ sont examinés, y compris les scénarios tels que les cordes cosmiques, les interactions de particules exotiques ou les composants supplémentaires de matière noire. L'étude se penche également sur les efforts en cours et les défis posés par l'observation du signal global de $21cm$, ainsi que sur la complexité de l'élimination des avant-plans.

En outre, les techniques d'estimation des paramètres sont discutées, mettant en évidence les méthodologies employées pour extraire des informations astrophysiques précieuses des données $21cm$ observées. Enfin, cette thèse se concentre sur une méthode spécifique d'estimation des paramètres, qui adopte les combinaisons de la chaîne de Markov Monte Carlo (MCMC) avec l'algorithme de Levenberg Marquardt (LM) pour estimer les paramètres physiques les mieux ajustés des courbes de $21cm$. La méthode ARES (Accelerated Reionization Era Simulations) est utilisée pour générer des modèles théoriques du signal global de $21cm$. Cette méthode offre un contrôle complet sur les paramètres de l'algorithme, permettant d'opter pour n'importe quelle combinaison de paramètres disponibles dans le cadre de l'ARES.

La connaissance de ces paramètres les mieux adaptés devrait permettre de contraindre les modèles proposés à l'avenir et de fixer des limites théoriques pour la précision des expériences à venir afin d'observer les effets non standard souhaités.

Acknowledgements

I would like to express my gratitude to my supervisors, Jonathan Sievers and Oscar Hernandez, for their invaluable help and patience throughout this project. I must acknowledge Jordan Mirocha for developing the ARES code and responding to my questions on my specific application of this package. I would like to thank the *Digital Research Alliance of Canada* for offering the computational resources needed for the analysis of this thesis.

I am deeply grateful to my parents for their unwavering support and enthusiasm. Even though we were thousands of kilometers apart, I could always rely on them being there for me. They kept me motivated during my hard days by reminding me of my reasons for pursuing physics academically. I wish that one day I will be able to return their kindness.

Additionally, I want to thank my roommates and new friends in Montreal for the joyful moments, unique adventures, and wonderful experiences we shared. Our late-night scientific debates were an inspiration for my research.

Furthermore, I would like to acknowledge the significant role of the staff at McGill

Wellness Hub. They kindly helped me to overcome the health issues I faced during my graduate journey. Their constant presence and willingness to support was a true blessing.

I learned a lot during the past two years, both scientifically and non-scientifically. To recap all the experiences in a sentence, I would say that I entered my master's as a young inexperienced girl, but I am leaving it as a grown-up educated woman.

Finally, I would like to dedicate this work to all lifelong learners and doers: you are changing the world every day!

Contents

1	Introduction	1
1.1	Background and motivation	2
1.2	Research questions and objectives	4
1.3	Overview of the thesis	5
2	The Global 21cm Signal	7
2.1	Theoretical basis of the 21cm signal	8
2.1.1	Physical Principles of the 21cm spectral line	8
2.1.2	Sky-Averaged 21cm Signal	11
2.2	Simulating the global 21cm signal	14
2.2.1	21cmFAST	16
2.2.2	The Accelerated Reionization Era Simulations (ARES)	17
2.3	Effects of non-standard physics on the global 21cm signal	20
2.3.1	Cosmic Strings	20

2.3.2	Dark Matter	20
2.3.3	Other non-standard effects	20
3	Observations of the Global 21cm Signal	21
3.1	Experiment to Detect the Global EoR Signature (EDGES)	23
3.1.1	error bars and foreground removal	23
3.1.2	theoretical model and associated parameters	23
3.2	Small Array for Research in Astrophysics of the South (SARAS)	23
4	Parameter Estimation Methods	24
4.1	Levenberg-Marquardt (LM)	25
4.1.1	Covariance Matrix	26
4.1.2	Derivation of the Levenberg-Marquardt Algorithm	29
4.2	Markov Chain Monte Carlo (MCMC)	31
4.2.1	Convergence Test	32
4.3	Combination of MCMC and LM	33
4.3.1	Generating correlated noise	34
4.4	Testing the Algorithm	35
4.4.1	The chi-square test	35
4.4.2	Chi-Square vs Parameters Plots	36
5	Results and Analysis	44

5.1	Key Astrophysical Parameters in the Global 21cm Signal	45
5.2	Parameter Estimation of an ARES generated curve	47
5.3	Parameter estimates of EDGES data and uncertainties	50
5.3.1	Choice of "multiplication factor"	50
5.3.2	error bar calculation	50
5.3.3	results	51
6	Discussion and Conclusion	69
6.1	Interpretation of the results	70
6.2	Summary of the main findings	70
6.3	Comparison with previous studies and observations	70
6.4	Contributions and significance of the research	70
6.5	Limitations	70
6.6	Future work	71
7	Appendices	72
7.1	Derivation of radiometer equation	72
7.2	Code snippets and scripts	72
7.2.1	Levenberg-Marquardt	72
7.2.2	Markov Chain Monte Carlo	72
7.2.3	drawing samples from covariance matrix	72

List of Figures

1.1	Spin-flip Transition of Neutral Hydrogen	3
2.1	Time evolution of the fluctuations in the 21cm brightness temperature	15
2.2	Evolution of the mean temperature generated using 21cmFAST	17
2.3	Typical global 21cm curve generated using ARES	19
4.1	Flow chart of LM	37
4.2	Flow chart of MCMC	38
4.3	An unconverged MCMC chain and its power spectrum	39
4.4	A converged MCMC chain and its power spectrum	39
4.5	Flow chart of the procedure to combine MCMC and LM	40
4.6	Corner plots of an MCMC chain	41
4.7	Histogram of difference in the chi-square values of drawn samples	42
4.8	Chi-Square vs parameters plots	43
5.1	Behaviour of global 21cm model with respect to chosen parameters	53

5.2	Histogram of distribution of samples	54
5.3	Histogram of Chi-Square of drawn samples	55
5.4	Chi-Square of Drawn samples vs parameter values	56
5.5	Chi-Square of Drawn samples vs parameter values, zoomed	57
5.6	Trend of parameters	58
5.7	Power spectrum of the chain	59
5.8	Trend of chi-square	60
5.9	Corner plots of the chain	61
5.10	Histogram of distribution of samples	62
5.11	Histogram of Chi-Square of drawn samples	63
5.12	Chi-Square of Drawn samples vs parameter values	64
5.13	Trend of parameters	65
5.14	Power spectrum of the chain	66
5.15	Trend of chi-square	67
5.16	Corner plots of the chain	68

List of Tables

5.1	Mean and standard deviation of samples	49
5.2	Results of fitting a known ARES curve with MCMC chain	50
5.3	Mean and standard deviation of samples	52
5.4	Results of fitting EDGES data with MCMC chain	52

List of Acronyms

ARES	The Accelerated Reionization Era Simulations.
CMB	Cosmic Microwave Background.
DLS	Damped Least-Squares.
EDGES	Experiment to Detect the Global EoR Signature.
EoR	Epoch of Reionization.
IGM	Intergalactic Medium.
LM	Levenberg-Marquardt.
MCMC	Markov Chain Monte Carlo.
PRIZM	Probing Radio Intensity at high-Z from Marion.
RTE	Radiative Transfer Equation.
SARAS	Small Array for Research in Astrophysics of the South.
SED	Spectral Energy Distribution.
SFR	Star Formation Rate.

Chapter 1

Introduction

21cm cosmology is a relatively new opened window in the study of the universe during its early stages of evolution. Its applications range from the study of cosmic dawn and epoch of reionization (EoR) to cosmic structure formation and dark matter investigations [1]. The field holds great potential for revolutionizing our understanding of the first stars, galaxies, and black holes by leveraging the temporal and spatial information embedded in the cosmic 21-cm signal [2].

In this chapter, we first will talk about the importance of this signal and its applications. Then, we will describe the motivations of this research to clarify the effects of non-standard physics on this signal ¹. Finally, in the last section of this chapter, we will briefly go over all the materials provided in this thesis.

¹It is worth emphasizing that in this thesis, we will only focus on the global 21cm signal as the subject of study.

1.1 Background and motivation

After the occurrence of the big bang, prior to the formation of the first stars and galaxies ($200 \lesssim z \lesssim 1100$), the universe was primarily composed of gas (with hydrogen constituting approximately 75% and helium, along with trace quantities of heavy elements, comprising the remaining portion). Additionally, there existed a comparatively smaller amount of free electrons relative to the gas, accompanied by the residual photons originating from the initial big bang, commonly referred to as the cosmic microwave background (CMB) [3, 4].

Since neutral hydrogen is the most frequent component of the intergalactic medium (IGM), it provides a convenient tracer for the behavior of baryonic matter in the early universe. Neutral hydrogen has a hyperfine splitting on its 1S ground state caused by the interaction between the magnetic moment of the proton and electron (Figure 1.1). This spin-flip transition results in the absorption or emission of a photon with the frequency of 1420.4057 MHz [5] corresponding to a wavelength of 21.1 cm [4].

Given that the CMB encompasses photons with the wavelength of 21 cm , hydrogen atoms are able to engage in interactions with the CMB, thereby facilitating the absorption of the 21 cm photon. This interaction takes place approximately during the dark ages and the EoR. As a consequence of this interaction, the brightness temperature of the 21 cm line experiences a notable alteration³. By employing modern radio interferometers equipped with precise

²The existence of this spectral line was theoretically predicted by van de Hulst in 1942 and the first ever detection was reported by Ewen and Purcell in 1951 [4].

³This interaction will be discussed in detail in Chapter 2 as the coupling of the spin temperature T_s with the kinetic temperature of the gas T_k .

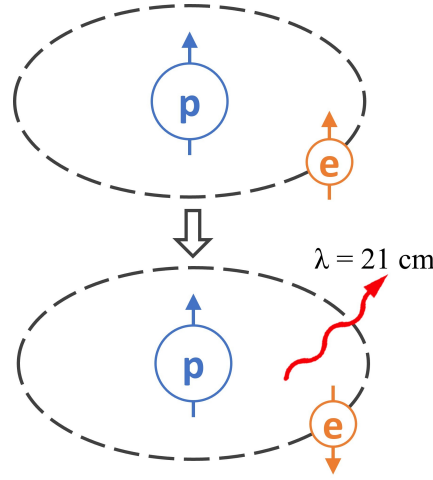


Figure 1.1: A basic depiction of the spin-flip transition on the ground energy state of the neutral hydrogen. The upper and lower plots indicate the triplet and singlet state respectively. The energy difference associated with this transition is $\Delta E = 5.9 \times 10^{-6} eV$ [4]. Figure from Kit Gerodias [6].

observation capabilities, this alteration can be effectively detected. It is worth noting that due to the redshift, the 21cm signal attains frequencies ranging from approximately 30 to 200 MHz , rendering it readily accessible to our radio interferometers [5]. These observations are capable of giving us valuable information about the distribution of neutral hydrogen and the evolution of cosmic structure over time [5].

The global 21cm signal is the average over the brightness temperature of the 21cm line across the entire sky. It is a measure of the overall state of the intergalactic medium (IGM) and presents as an excess absorption or emission in different redshift regions. This radiation is an observational evidence for certain characteristics of the IGM in the early universe (e.g., temperature, density, and reionization state). These properties are determined by

the complex interplay between the cosmic radiation field, the formation and evolution of the first stars and galaxies, and the feedback processes that these sources exert on their surroundings [4].

Besides all the above-mentioned applications, the global 21cm signal is a **strong probe for non-standard physics** during the dark ages. It has the potential to shed light on mysteries surrounding dark matter/dark energy, the existence of cosmic strings, and even certain particle interaction [7–11]⁴. This capacity of the global 21cm signal is the main motivation of this research.

1.2 Research questions and objectives

The effects of non-standard physics in 21cm signal have gained lots of attraction in the recent literature (cite) . These effects were investigated through the application of analytical and semi-analytical methods. However, the majority of the studies were predominantly analytical in nature, regardless of the observational data (citation).

We aim to fill this research gap by continuing the semi-analytical efforts to simulate the global 21cm signal with an aim to prob these non-standard effects. With the recently released data at one's disposal [12], we use certain fitting algorithms to compare them to theoretically simulated models [13]. The first step is to estimate the physical parameters of these curves by only taking the standard physical mechanisms into account.

⁴These effects will be discussed more in 2.3.

Add
these
citations

Add
these
citations

In future studies, we will include a realistic foreground model and upgrade our simulator to include desired non-standard effects. We will again fit the observational data to the upgraded version of the theoretical model to investigate patterns of change in the best-fit physical parameters. The insights from this study will be used to constrain the physical parameters found by newly proposed models. Moreover, it will empower us to determine whether the upcoming radio interferometers have enough precision to detect our targeted non-standard effects.

1.3 Overview of the thesis

This thesis consists of two major components: the literature review and the research.

In the literature review chapters (chapters 2 and 3), we first talk about the global 21cm signal and its physical principles. We continue by exploring the effects of non-standard physics on the global 21cm signal in the recent literature.

In chapter 3, we will briefly introduce all of the present and future observational projects aiming to detect the global 21cm signal. From all these experiments, we will thoroughly discuss the Experiment to Detect the Global EoR Signature (EDGES) and the Small Array for Research in Astrophysics of the South (SARAS)⁵.

In the research half of this thesis (chapters 4 and 5), we place a stronger emphasis on

⁵The selection of these two experiments is justified by their explicit emphasis on observing the global 21cm signal rather than spatial fluctuations, coupled with the availability of their released data.

computational aspects. In chapter 4, we examine the importance of estimating the parameters of the global 21cm signal and how these estimations affect future proposed theoretical models and observations. Furthermore, we briefly describe different methods used to serve this purpose and the advantages of each one. Subsequently, we will Bring forth the details of the specific method used in this study. Chapter 5, demonstrates the results of applying this computational method to EDGES observational data.

Finally, in chapter 6, we interpret the outcome and talk about the implications of these results for cosmology and astrophysics. Also, the limitations and the future prospective of the project is mentioned in this chapter.

Chapter 2

The Global 21cm Signal

As previously mentioned, the global 21cm signal is a new window to extract data and build a better understanding of the early universe. To achieve this goal, we need to carefully construct the physical theory, try to simulate the signal, build radio telescopes to observe it and finally, analyse the observational data and compare them to our theoretical models.

In this chapter, we will present the latest findings about the physical background, simulations and effects of non-standard physics on global 21cm signal. In the last section of this chapter, we will talk about the importance of parameter estimation and its methods.

In chapter 3, we will talk about the attempts of observing this signal and foreground removal challenges.

2.1 Theoretical basis of the 21cm signal

2.1.1 Physical Principles of the 21cm spectral line

The characteristics of the 21cm line depends on the radiative transfer along the line sight.

To find the brightness temperature of the 21cm line, we start by the basic radiative transfer equation for the specific intensity I_ν :

$$\frac{dI_\nu}{ds} = -\alpha_\nu + j_\nu \quad (2.1)$$

Where α_ν and j_ν are absorption and emission coefficients respectively. It is essential to note that this equation is written under the assumption of zero scattering.

We work in the Rayleigh Jeans limit, which gives us: $I_\nu = 2k_B T \nu^2 / c^2$. We also know that the absorption coefficient α_ν can be related to the definition of optical depth along the line of sight: $\int ds \alpha_\nu(s)$ where ds is a path length. Now, we may rewrite equation 2.1 to find the observed brightness temperature T_b^{obs} at a frequency ν along the line of sight from a background radio source through a cloud of optical depth τ_ν and uniform excitation temperature T_{ex} :

$$T_b^{obs} = T_{ex} (1 - e^{-\tau_\nu}) + T_R(\nu) e^{-\tau_\nu} \quad (2.2)$$

For 21cm applications, the excitation temperature is known as spin temperature T_S . The definition of spin temperature is dependant on the number densities of hydrogen atoms in

triplet (n_0) and singlet state (n_1).

$$\frac{n_1}{n_0} = \frac{g_1}{g_0} e^{-\frac{T_*}{T_S}} \quad (2.3)$$

$$g_0 = 1, g_1 = 3 \quad (2.4)$$

$$T_* \equiv \frac{E_{10}}{K_B T_S} = \frac{hc}{k\lambda_{21cm}} = 0.068K \quad (2.5)$$

where $g_1/g_0 = 3$ is the ratio of the statistical degeneracy factors of the two levels, and $T_* \equiv hc/k\lambda_{21cm} = 0.068K$. With this definition, the optical depth of a cloud of hydrogen is then

$$\tau_\nu = \int ds \left[1 - e^{-\frac{T_*}{T_S}} \right] \sigma_0 \phi(\nu) n_0, \quad (2.6)$$

Where $n_0 = n_H/4$ with n_H being the hydrogen density, and we have denoted the 21cm cross-section as $\sigma_0 \equiv 3c^2 A_{10}/8\pi\nu^2$, where $A_{10} = 2.85 \times 10^{-15} s^{-1}$ is the spontaneous decay rate of the spin-flip transition, and the line profile normalized so that $\int \phi(\nu) = 1$. A_{10} is a very small rate. Rare occurrence of the transition implies that the faintness of the 2cm signal [6]. The deviation of the spin temperature from the background temperature will be the key that makes this signal detectable¹. Thus, in the study of physics of 21cm signal, we mainly focus on the fluctuations of the spin temperature.

Three competing processes influence the spin temperature: 1) interaction of 21cm photons

¹Although it is possible to choose a radio-loud point source as the background, but since the order of fluctuations in the CMB temperature is insignificant in our study ($\delta T_{CMB} \approx 10^{-5}$), the CMB is a great candidate as a source of uniform brightness [4].

with the background (mostly CMB), 2) collisions with other particles (hydrogen atoms, free electrons and protons [5] but mostly hydrogen atoms), and 3) resonant scattering of $Ly\alpha$ photons that cause a spin-flip with the meddling of an intermediate excited state. Therefore, the spin temperature can be found using the equilibrium between these mechanisms and their corresponding Einstein coefficients. After simplifications, we have:

$$T_S^{-1} = \frac{T_\gamma^{-1} + x_\alpha T_\alpha^{-1} + x_c T_K^{-1}}{1 + x_\alpha + x_c} \quad (2.7)$$

Where T_γ is the temperature of the surrounding bath of radio photons ($T_\gamma = T_{CMB}$). T_α is the color temperature of the $Ly\alpha$ radiation field at the $Ly\alpha$ frequency and is closely coupled to the gas kinetic temperature T_K by recoil during repeated scattering. x_c and x_α are the coupling coefficients due to atomic collisions and scattering of $Ly\alpha$ photons, respectively. The spin temperature becomes strongly coupled to the gas temperature when $x_c + x_\alpha \gtrsim 1$ and relaxes to T_γ when $x_c + x_\alpha \ll 1$.

Wouthuysen-Field Coupling

As previously mentioned, a hydrogen atom in the early universe can interact with CMB photons that had frequencies matching the energy gaps of hydrogen atoms, especially in the $Ly\alpha$ band. However, with the onset of star formation, CMB will no longer be the only source of photons for the hydrogen atom to interact with. The newly formed compact objects are capable of generating UV photons, including $Ly\alpha$, and reheating the IGM. These photons

are injected into the $Ly\alpha$ frequency band by resonant scattering rather than being redshifted from outside the line. The existence of this second channel increases the coupling ability of the hydrogen-background interaction, further assisting the spin temperature T_S in coupling to T_K .

The process of coupling the spin temperature of neutral hydrogen to the background radiation $Ly\alpha$ is called **Wouthuysen-Field Coupling** [14]². This process plays a pivotal role in the observability of the global 21cm signal during dark ages by forcing the signal to deviate from the temperature of the CMB.

The $Ly\alpha$ coupling coefficient can be written as a function of scattering rate P_α [5]:

$$x_\alpha = \frac{4P_\alpha}{27A_{10}} \frac{T_*}{T_\gamma} \quad (2.8)$$

2.1.2 Sky-Averaged 21cm Signal

Based on the discussions of the last section, the equation for the sky-averaged 21cm signal can be written as [5]:

$$\delta T_b \approx 27 (1 - \bar{x}_i) \left(\frac{\Omega_{b,0} h^2}{0.023} \right) \left(\frac{0.15}{\Omega_{m,0} h^2} \frac{1+z}{10} \right)^{1/2} \left(1 - \frac{T_\gamma}{T_S} \right) \quad (2.9)$$

²The Wouthuysen-Field effect is named after two physicists who independently described the phenomenon in 1952 and 1958: Robert H. Wouthuysen [15], and George B. Field [16].

Where x_i is the ionization fraction, h is the dimension-less Hubble constant, $\Omega_{b,0}$ and $\Omega_{m,0}$ are the current ratio of the energy density of baryonic and total matter to the critical density of the universe.

To describe the fluctuations of global 21cm through the thermal history of the universe and the physical mechanisms behind them, we split the early universe era into different redshift regions:

- $200 \gtrsim z \gtrsim 1100$: Compton scattering maintains the thermal coupling of gas to the CMB temperature through the residual free electrons after the recombination ($T_K = T_\gamma$). Due to the high density of the gas, the collisional coupling is dominant, forcing the spin temperature to the kinetic temperature of the gas. Therefore, the brightness temperature of the 21cm signal is zero during this redshift regime [4].
- $40 \gtrsim z \gtrsim 200$: The universe becomes cool enough for subatomic particles to combine and form neutral hydrogen. As a result, baryonic matter experiences thermal decoupling from the CMB, making it possible for the non-relativistic gas to cool adiabatically with the expansion of the universe [4]. The temperature of the gas and CMB drops as $T \propto a^{-2}$ and $T \propto a^{-1}$ respectively³. This rate discrepancy leaves the gas cooler than radiation while effectively stopping heat exchange between these two components. As a result, the gas spin temperature decouples from the CMB temperature. Since the effect of collisional coupling is still significant, we have

³" a " is the expansion scale factor

$T_S = T_K$. Consequently, the 21cm brightness temperature becomes negative (compared to the CMB background) in the average spectrum corresponding to this redshift [3, 4].

- $z_* \lesssim z \lesssim 40^4$: As the density keeps dropping through the expansion, the influence of collisional couplings becomes less significant, causing the spin temperature to again couple with the CMB temperature ($T_S \rightarrow T_\gamma$). Thus, the 21cm brightness signal goes back to zero again [3]. The first blue regions in the upper panel of figure 2.1 and corresponding absorption through in the lower panel depict the above-mentioned process [3, 4].
- $z_\alpha \lesssim z \lesssim z_*$: The second fluctuation in figure 2.1 emerged through the formation of the first stars and galaxies. As large halos begin to collapse to form first stars and galaxies, they generate both x-ray and $Ly\alpha$ emissions. Two mechanisms create the $Ly\alpha$ photons: 1) Continuum radiation redshifted to the $Ly\alpha$ wavelength and 2) Ionization and deexcitation of IGM gas. Since the emissivity required for the $Ly\alpha$ coupling is less significantly less than that for heating T_k above T_γ , the spin temperature tends to couple to cold gas ($T_S \rightarrow T_K$) through the Wouthuysen-Field effect. Therefore, we will again observe the 21cm absorption through [3, 4].
- $z_r \lesssim z \lesssim z_\alpha$: Eventually, the gas is reheated by ionizing x-ray photons from galaxies [4],

⁴There is still considerable uncertainty in the exact values of this redshift range and the sequence of events due to our ignorance of early sources. This uncertainty is such significant that there might even be an overlap between the regions discussed above [4].

and the 21cm brightness temperature goes back to zero (second absorption through in the lower panel of figure 2.1). The influence of this reheating mechanism is such strong that we even expect to observe 21cm emission in this redshift range (red region in the upper panel of figure 2.1). From this point on in the thermal history of universe, we do not expect to see anymore 21cm signal from IGM since most of the gas will be ionized by emergent stars, galaxies and accreting blackholes. Therefore, the 21cm brightness temperature goes to zero (the black region in the upper panel of figure 2.1). However, in the regions with higher recombination rate inside galaxies and dark matter halos, the neutral hydrogen is shielded and preserved. Thus, the 21cm signature originating from inside the galaxies will continue to exist [3, 4].

2.2 Simulating the global 21cm signal

With the advancement of radio telescopes, we have entered a data-driven era in 21-cm cosmology, which allows us to place constraints on the properties of astrophysical sources responsible for generating this signal. Nevertheless, extracting astrophysical insights from the collected data is a complex task that necessitates the generation of theoretical templates that span various astrophysical parameters in a fast and efficient manner [18]. In order to do so, fully hydrodynamic simulations of the 3D evolution of the brightness temperature of the 21cm spectral line have been proposed previously [2]. However, these simulations are

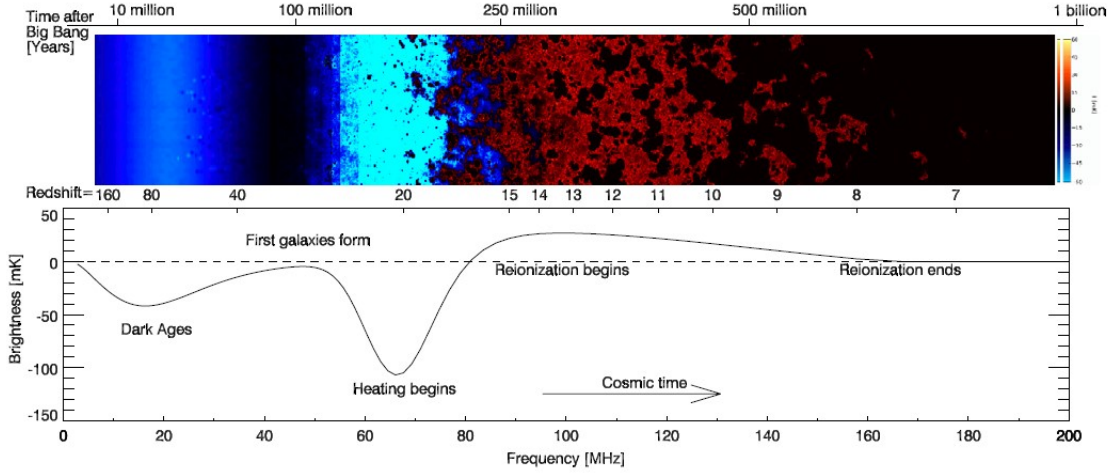


Figure 2.1: Time evolution of the fluctuations in the 21cm brightness temperature (solid line) compared to the CMB background (dashed line). The top panel is a color plot showing fluctuations arising from variation in density. The coloration clearly shows the two absorption phases of 21cm brightness temperature (coupling of T_S to T_K , blue), emission phase (red), and the regions where it disappears completely (coupling of T_S to T_γ , black). The lower panel represents the evolution of sky-average (global) 21cm signal from the dark ages to the reionization. The frequency range of the absorption and emission regions exactly matches the corresponding regions in the upper panel. Figure from Pritchard and Loeb, 2011 [4]. The precise details of the shape of this signal are still unidentified due to our lack of knowledge on the nature of first galaxies [17].

computationally expensive, and this issue will considerably limit our ability to search the parameters space [13]. To solve this, a middle-ground solution between these simulations and fully analytical studies has been proposed: semi-analytical methods. The results of these semi-analytical calculations are comparable to hydrodynamic simulation and consume a significantly lower amount of run-time.

In this section, we introduce two powerful tools capable of simulating the theoretical 21cm

curve. The first one is 21cmFast which calculates the global 21cm curve by averaging over all of the spatial fluctuations. Another one is The Accelerated Reionization Era Simulations (ARES), which straightly calculates the global curve by using a novel approach to solving the cosmological radiative transfer equation (RTE) [13]. Although 21cmFast is perfectly capable of doing the same job as ARES, we will use 21cmFast in our analysis, since the utilization of 21cmFast is excessive for generating the global 21cm curve.

2.2.1 21cmFAST

21cmFAST is a Python-integrated C package designed to produce 3D cosmological realizations of physical fields playing a role in the early universe. It is based on a semi-numerical approach combining the excursion set formalism with perturbation theory. 21cmFAST is capable of simulating the 3D realizations of density, peculiar velocity, halo, ionization, spin temperature fields, 21cm , and ionizing flux fields⁵⁶ [2, 19].

As mentioned above, the original simulation was developed as a C script. Later, in 2020, the equivalent Python package was introduced as the third version of 21cmFAST. The core C code is a high-performance script that uses the excursion set formalism to identify regions of ionized hydrogen atop a cosmological density field evolved using first- or second-order Lagrangian perturbation theory, tracking the thermal and ionization state of the intergalactic medium, and computing X-ray, soft UV, and ionizing UV cosmic radiation fields based on

⁵Documentation: <https://21cmfast.readthedocs.io/en/latest/>

⁶GitHub Repository: <https://github.com/21cmfast/21cmFAST>

parameterized galaxy models [2].

An example of a mean temperature curve generated using 21cmFAST is shown in 2.2.

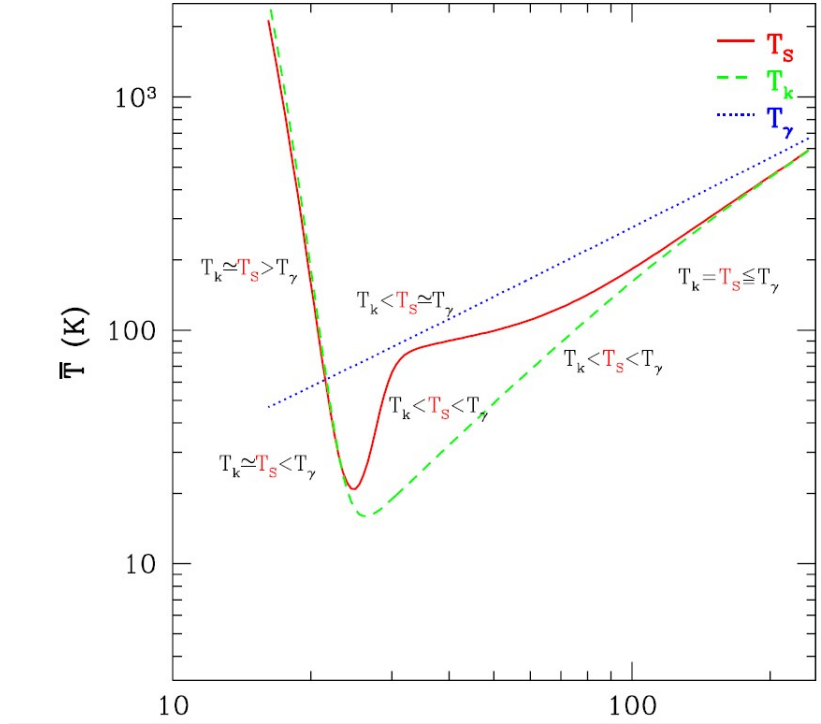


Figure 2.2: Evolution of mean the temperature generated using 21cmFAST. Solid, dashed and dotted curves represent the spin temperature, the kinetic temperature of the gas, and CMB temperature (equivalent to background temperature in 21cm applications) respectively. Figure from [19]

2.2.2 The Accelerated Reionization Era Simulations (ARES)

The Accelerated Reionization Era Simulations, or in the short form *ARES*, is a Python package for quick and efficient generation of 21cm curves^{7 8} [13]. Alongside global 21cm curve

⁷Documentation: <https://ares.readthedocs.io/en/latest/>

⁸GitHub Repository: <https://github.com/mirochaj/ares>

applications, it can be used for stand-alone non-equilibrium chemistry solver, global radiation background calculator, galaxy semi-analytic modeling [20–22], PopIII star modeling [23], 1D radiative transfer, and spectral energy distribution (SED) optimization [24].

ARES draws the globally-averaged 21cm curve through the numerical calculation of equation 2.9. To do so, we need to evaluate the spin temperature T_S , which is dependent on coupling coefficients x_α and x_c . The collisional coupling x_c is found using the tabulated values in [25], and the $Ly\alpha$ coupling coefficient is calculated using equation 2.10. By ignoring detailed line profile effects, this expression can be written in the following form [26–28] as a function of the angle-averaged $Ly\alpha$ back-ground intensity \hat{J}_α which determines the strength of Wouthuysen-Field coupling [13]:

$$x_\alpha = 1.81 \times 10^{11} \frac{\hat{J}_\alpha}{1+z} \quad (2.10)$$

Where \hat{J}_α itself can be written using the general definition of angle-averaged back-ground intensity as a function co-moving volume density [13]:

$$\hat{J}_\nu(z) = \frac{c}{4\pi} (1+z)^2 \int_z^{z_f} \frac{\hat{\epsilon}_{\nu'}(z')}{H(z')} e^{-\bar{\tau}_\nu} dz' \quad (2.11)$$

Numerical evaluation of this expression is generally computationally heavy, mostly due to the optical depth (τ_ν) term. One solution is to tabulate the optical depth values on an

⁹In this expression the $\hat{J}_\nu(z)$ and $\hat{\epsilon}_{\nu'}$ are in units of photon number density: $[\hat{J}_\nu] = \text{s}^{-1} \text{ cm}^{-2} \text{ Hz}^{-1} \text{ sr}^{-1}$, $[\hat{\epsilon}_\nu] = \text{s}^{-1} \text{ Hz}^{-1} \text{ cMpc}^{-3}$.

arbitrary number of redshift points. However, the accuracy of this method is dependent on the number of chosen redshift points in the look-up table, and undersampling might result in large deviations in background radiation intensity.

ARES uses the above-mentioned approach to evaluate equation 2.9 and simulate the global 21cm curve. A typical ARES-generated global 21cm curve is presented in 2.3.

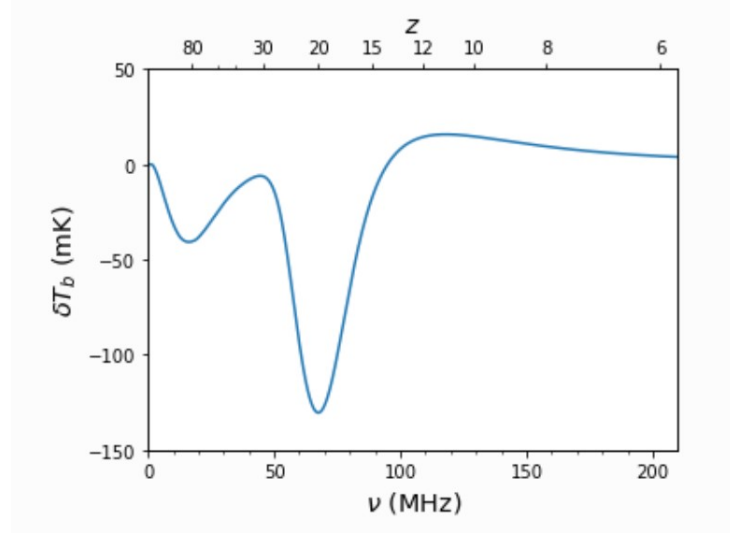


Figure 2.3: An example of a global 21cm signal generated using ARES, illustrating the evolution of the brightness temperature of 21cm line against the background radio sources as a function of frequency. The fluctuations discussed in section 2.1.2 are perfectly demonstrated in the simulated signal. Note the similarities to corresponding regions in figure 2.1. Figure from Jordan Mirocha in the ARES documentation

2.3 Effects of non-standard physics on the global 21cm signal

2.3.1 Cosmic Strings

[9] [29] [30]

2.3.2 Dark Matter

[8] [31] [32] [33] [7]

2.3.3 Other non-standard effects

[10] [11]

Chapter 3

Observations of the Global 21cm

Signal

List of experiments (reminder: rephrasing and citing each of them, things that I need for each experiment: dipole antenna, location, time frame of results, frequency range), only mention the global 21cm ones not all 21cm:

why is it hard: Unavoidable (beam-averaged) foregrounds which are ~ 10 times larger than the signal. • Beam chromaticity mixes spatial and spectral structure of the foregrounds with that of the instrument. • Also: Ionospheric effects (see Datta et al. 2016), RFI, radio Solar emissions.

While most experiments in this field focus on spatial fluctuations of the 21cm signal to study the large-scale structure of the universe, there are a few experiments specifically

designed to detect the global 21cm signal:

1. EDGES (Experiment to Detect the Global EoR Signature): This was the first experiment to report a detection of the global 21cm signal in 2018, by measuring the absorption of radio waves from distant sources by neutral hydrogen in the intergalactic medium [12].
2. SARAS (Small Array for Research in Astrophysics of the South): This is a radio telescope located in India that has been used to study the global 21cm signal since 2015.
3. PRIZM [34] (Probing Radio Intensity at high-Z from Marion): is an experiment that has been designed to study cosmic dawn in the universe using 50-150 MHz observations of globally averaged 21-cm emission. The experiment consists of two modified four-square antennas, operating at center frequencies of 70 and 100 MHz, and a dual-polarization spectrometer back end. PRIZM deployed in April 2017 to Marion Island, an exceptionally isolated and radio-quiet location in the sub-Antarctic, and science observations are currently in progress. initially called SCI-HI (Small Radio Telescope for Cosmic Hydrogen Intensity Mapping)
4. REACH (Radio Experiment for the Analysis of Cosmic Hydrogen)
5. SKA [35]

6. BIGHORNS (Broadband Instrument for Global HydrOgen ReioNisation Signal): This is a radio interferometer located in Australia that was designed to detect the global 21cm signal during the epoch of reionization.

3.1 Experiment to Detect the Global EoR Signature (EDGES)

put a picture of the antenna

3.1.1 error bars and foreground removal

3.1.2 theoretical model and associated parameters

3.2 Small Array for Research in Astrophysics of the South (SARAS)

put a picture of the antenna

Chapter 4

Parameter Estimation Methods

talk about different methods used to serve this purpose and advantages of each one

Now that we have talked about the theoretical global 21cm signal and the attempts to observe it, we shall proceed by talking about the parameter estimation of this signal. Various computational algorithms, including machine learning and neural networks, have been used to accomplish this task (cite) . While neural networks have been shown to be effective, certain drawbacks put sampling algorithms like MCMC on an advantaged position for global 21cm applications.

Sampling algorithms like MCMC allow us to map out the full likelihood surface which in our case, is achievable. However, neural nets are usually preserved for problems in which mapping the whole likelihood surface becomes too complicated. In this chapter, we describe the main fitting algorithm used in our study, which combines Levenberg-Marquardt and

Add
the
citation

mention
which
draw
backs

MCMC. We explain the reason behind utilizing both of these algorithms for this particular fitting challenge and provide a detailed explanation of the procedure to combine them. We also discuss two different tests used to measure the quality of the proposed fit.

In chapter 5, we present the results of applying this fitting method to the observed global 21cm curve¹ and its corresponding theoretical model².

4.1 Levenberg-Marquardt (LM)

The Levenberg-Marquardt (LM) algorithm, also known as the damped least-squares (DLS) method, is a fitting algorithm used for non-linear least-squares problems. This iterative algorithm is based on another root-finding method referred to as "Newton's method".

LM is perfectly capable of fitting models with Gaussian-shaped likelihood spaces. However, it's abilities are limited when it comes to fitting error bars.

We continue this chapter by deriving the basic analytical definition of this method. In order to do so, we start by defining the matrix form of chi-square. Subsequently, we attempt to calculate the second order derivative of chi-square with respect to the parameters of the model. We will show that this calculation leads to defining the covariance matrix, which will be later used as our basis to generate correlated noise for the MCMC algorithm.(4.3.1).

¹released by the EDGES group

²generated using ARES

4.1.1 Covariance Matrix

A traditional fitting problem is normally defined as trying to find the theoretical model which can best explain a set of data and its associated noise. The quality of this fit is usually measured by the value of likelihood. If we assume the noise to be Gaussian, the effort to maximize the likelihood in the presence of Gaussian noise leads to the minimization of the following expression called the "chi-square":

$$\chi^2 \equiv (d - A(m))^T N^{-1} (d - A(m)) \quad (4.1)$$

Where d is the array containing the data points and A is the model which is dependent on the set of parameters m (the dependency can be nonlinear). Thus, $A(m)$ gives the expected value of the data with respect to the theoretical model. N is also defined as the noise matrix which in general can be non-diagonal. The above definition is written in the language of linear algebra.

In the case of a diagonal noise matrix, expression 4.1 takes the following form:

$$\chi^2 = \sum \frac{(x_i - \mu_i)^2}{\sigma_i^2} \quad (4.2)$$

Where x_i is the observed data, μ_i is the expected value ($\mu_i = \langle d_i \rangle = A_i(m)$), and σ is the error associated with each data point ($N_{i,i} = \sigma_i^2$).

We continue by calculating the first two derivatives of the above expression, leading to

the construction of the gradient decent method.

$$\frac{d\chi^2}{dm} = - \left(\frac{dA(m)}{dm} \right)^T N^{-1} (d - A(m)) - (d - A(m))^T N^{-1} \left(\frac{dA(m)}{dm} \right) \quad (4.3)$$

We define $A' \equiv \frac{dA(m)}{dm}$, and $r \equiv d - A(m)$. Thus the above expression takes the form:

$$\frac{d\chi^2}{dm} = - (A')^T N^{-1} r - r^T N^{-1} A' \quad (4.4)$$

Since we know that:

$$(N^{-1})^T = N^{-1} \quad (4.5)$$

$$[A' N^{-1} r]^T = r^T N^{-1} (A')^T \quad (4.6)$$

Substituting in 4.4, we get:

$$\frac{d\chi^2}{dm} = -2 (A')^T N^{-1} r \quad (4.7)$$

Thus, we can calculate the second derivative:

$$\frac{d^2\chi^2}{dm^2} = -2 \left(\frac{dA'}{dm} \right)^T N^{-1} r - 2 (A')^T N^{-1} (-A') \quad (4.8)$$

It is usually safe to ignore the first term since the r component, which is the residual of

comparing the model to data, can take both negative and positive values; Thus on average, it will be close to zero. The deeper reason behind this neglecting is that our ultimate desire is to set the gradient of chi-square to zero. Therefore, it is still accepted if the curvature is slightly off, as long as we reach the maximum of likelihood ³.

Finally, using the above mentioned logic, we are left with:

$$\frac{d^2\chi^2}{dm^2} = 2 (A')^T N^{-1} A' \quad (4.9)$$

Which is the definition of the curvature matrix . Our primary focus lies not on the matrix itself, but rather on its inverse. The inverse is called the **Covariance Matrix**⁴. The diagonal elements of this matrix are simply the variance on each parameter ($\sigma_{i,i}$), while the off-diagonal elements represent the covariance, measuring the dependency of a pair of parameters ($\sigma_{i,j}$).

In general, we expect the covariance matrix to be semi-positive definite⁵.

³As mentioned before, we are only using LM to generate a covariance matrix for our MCMC. As a result, the calculated covariance matrix does not need to be perfect.

⁴The dimensions of this square matrix is the same as that of m .

⁵A positive definite matrix only posses positive eigenvalues. However, for a semi-positive definitive matrix, eigenvalues are non-negative.

4.1.2 Derivation of the Levenberg-Marquardt Algorithm

In LM method, on each iteration, the set of parameters m is replaced with $m + \delta m$. To find the δm , the function $\chi^2(m + \delta m)$ is approximated by its linearization:

$$\chi^2(m) = r^T N^{-1} r \quad (4.10)$$

$$\chi^2(m + \delta m) = \chi^2(m) + \left(\frac{d\chi^2}{dm} \right) \delta m \quad (4.11)$$

Similar to the procedure done in section 4.1, we calculate the derivative of 4.11:

$$\frac{d\chi^2(m + \delta m)}{dm} = \frac{d}{dm} (\chi^2) + \frac{d}{dm} \left(\frac{d\chi^2}{dm} \delta m \right) \quad (4.12)$$

We already have the expression for the first order derivative of chi-square in 4.4. Therefore:

$$\frac{d\chi^2(m + \delta m)}{dm} = -2 (A')^T N^{-1} r + \left(\frac{d^2\chi^2}{dm^2} \right) \delta m + \frac{d\chi^2}{dm} \left(\frac{d}{dm} (\delta m) \right) \quad (4.13)$$

Where the last term equals zero since δm does not have any fundamental dependencies on m .

Looking at the second term, it is simply inferred that we have already found the expression for second derivative of chi-square in 4.9. Thus, we are left with:

$$\frac{d\chi^2(m + \delta m)}{dm} = -2 (A')^T N^{-1} r + 2 (A')^T N^{-1} A' \delta m \quad (4.14)$$

Setting $\frac{d\chi^2(m+\delta m)}{dm} = 0$, we get:

$$A'^T N^{-1} A' \delta m = A'^T N^{-1} r \quad (4.15)$$

$$\delta m = \left(A'^T N^{-1} A' \right)^{-1} A'^T N^{-1} r \quad (4.16)$$

Equation 4.16 represents the basis for **Newton's method**. However, as previously mentioned, this method suffers from convergence issues, especially on complicated likelihood surfaces. To overcome this obstacle, we add a new term to the left-hand side of 4.16. This term includes a control parameter Λ that is updated on each iteration depending on the quality of fit.

$$\left(A'^T N^{-1} A' + \Lambda I \right) \delta m = A'^T N^{-1} r \quad (4.17)$$

$$\delta m = \left(A'^T N^{-1} A' + \Lambda I \right)^{-1} A'^T N^{-1} r \quad (4.18)$$

Now the basic idea is apparent: On each iteration, a set of parameters m will be replaced by $m + \delta m$ and the chi-square is calculated based on the perturbed parameters. Subsequently, the new chi-square is compared to its value in the last step. If we encounter a higher value, the Λ will be multiplied to a constant arbitrary number (> 1). Otherwise, it will be divided with another constant value (> 1). For practical purposes, if Λ takes a value lower than a constant small arbitrary number, we set it equal to zero. If the Λ is zero, and the chi-square

is less than an arbitrary threshold value, we declare the **convergence** of the algorithm.

A flow chart summary of this method is shown in 4.1. The Python code for LM is also available in appendix 7.2.1.

4.2 Markov Chain Monte Carlo (MCMC)

Given that Levenberg-Marquardt (LM) is not always effective in finding the best-fit point for complex likelihood spaces, a more powerful algorithm such as Markov Chain Monte Carlo (MCMC) is necessary in many real-life applications.

MCMC is particularly effective in fitting non-Gaussian likelihood spaces and has a guaranteed convergence, regardless of the starting point in parameter space. However, the algorithm is computationally heavy due to its iterative nature, which is based on the evaluation of chi-square on each step. Initially, an arbitrary point in parameter space is given to MCMC as its initial trial step and the associated chi-square is calculated. Then, a random point is drawn from a Gaussian distribution, where the mean is set at the last point in the chain⁶. Subsequently, the new chi-square is compared to the previous one from the last trial step. If the new chi-square is lower, the new trial point is accepted in the chain. If the new chi-square is higher, the trial point is accepted with a probability determined by a specific criterion.

⁶In Python applications, the `numpy.randn` function is used to serve this purpose.

The above-mentioned probability threshold is typically defined as:

$$Probability = e^{\frac{-1}{2}(\chi_{new}^2 - \chi^2)} \quad (4.19)$$

Which again has Gaussian insights.

As a measure of MCMC performance, the acceptance ratio is used to determine the fraction of trial steps that end up getting accepted into the chain. An ideal MCMC would typically have an acceptance ratio of 25 percent. However, even with a lower acceptance ratio, the MCMC can still converge, but it will require more trial steps.

A visual summary of MCMC algorithm is shown in 4.2, and the Python code is available at 7.2.2.

4.2.1 Convergence Test

The MCMC algorithm is designed to explore different regions of the parameter space in order to reach convergence. Various methods have been developed to ensure that the MCMC has converged, one of which is to check the power spectrum.

The power spectrum represents the distribution of power at different frequencies in the MCMC chain. A converged MCMC chain must have the behaviour of a white noise, with power uniformly distributed among all frequencies. On the other hand, an unconverged chain will show more power at lower frequencies compared to higher ones. Therefore, the criterion

for checking the convergence of an MCMC chain is the flatness of the power spectrum in low frequencies when plotted on a log-log scale. Figure 4.3 and 4.4 illustrates the difference between a converged and an unconverged chain.

4.3 Combination of MCMC and LM

As mentioned before, MCMC is a computationally heavy algorithm due to its iterative nature. If calculating the chi-square takes a long time on each step, the MCMC itself will have a rather long run time before reaching the converged state. Different methods have been proposed to deal with this issue (citation) and help the MCMC to converge faster, one of which is to use the insights from running LM ⁷.

We previously discussed that parameters of a model might be correlated (4.1.1). During a simple MCMC, we draw random samples from independent one-dimensional Gaussian distributions for each of the parameters. This samples do not take the possible correlations of parameters into account. On the other hand, generating samples using multivariate Gaussian distribution (joint normal distribution), will give us the capacity to encompass such characteristics. Eventually, the probability of them getting accepted into the actual chain will be higher. Eventually, we are able to summarize that this approach (feeding the MCMC with a posterior distribution) will eventually assist the MCMC to explore more

⁷It worth to again mention that our sole rationale to use LM in our application is to generate a covariance matrix for the MCMC.

efficient regions of parameter space, and converge faster. Figure 4.5 illustrates this technique briefly.

Since the covariance matrix of these needed samples is already in hand, we are able to easily generate a set of correlated noise samples from that. This procedure is described in the following section.

4.3.1 Generating correlated noise

As discussed before, the off-diagonal elements of a covariance matrix correspond to the inverse of covariance between each pair of parameters. Thus, if we draw samples from the inverse of covariance matrix (which needs to be calculated at the point of "best-fit"), we are essentially sampling from the multivariate normal distribution with the deviation values describing the uncertainties in the parameters⁸.

The equivalent methods can be used to generate correlated noise: Cholesky and eigenvalue decomposition⁹. For practical reasons, we prefer to use the eigenvalue decomposition for 21cm applications. The procedure is as follows: A matrix of normal gaussian-drawn random variables is constructed in the desired shape ($n \times m$, corresponding to the number of samples and number of parameters respectively). Then, it is multiplied by the eigenvalue matrix and scaled by the square root of the eigenvalues. The transpose of

⁸Figure 4.6, which shows the corner plots for a four-variable gaussian model, emphasizes the importance of sampling from a multivariate normal distribution and taking the correlations between the parameters into account.

⁹Normally, calculating the Cholesky decomposition takes a shorter amount of time.

the product will give us the correlated samples.

To gain more precision, is it possible to use the eigenvalues decomposition of the normalized covariance matrix (where diagonal samples all equal unity). The normalization process is done by multiplying the covariance matrix with its own diagonal. Eventually, the drawn samples need to be scaled by the square root of the diagonal matrix.

The Python implementation of the above-mentioned procedure is given in 7.2.3.

4.4 Testing the Algorithm

The complicated algorithm described in the previous sections, does not always behave as expected. Thus, naturally, one seeks options to weigh the output. In sections 4.4.1 and 4.4.2, we introduce two methods to measure the overall quality of the model fitting.

4.4.1 The chi-square test

This method is more focused on inspecting the output of LM and drawn samples. A large number of samples are drawn from the covariance matrix and the corresponding chi-squares are calculated. Since the covariance matrix describes the uncertainties in the parameters, we expect that the average difference in the chi-square statistics for two different samples should be of order unity per each parameter. This comes from the fact that the chi-square statistic scales with the uncertainties in the data and model, which are typically of order 1.

Figure 4.7 shows an example of the distribution of difference between the chi-square

values.

4.4.2 Chi-Square vs Parameters Plots

Another method to verify the results is to plot the chi-square values of drawn samples versus the each of the parameters. According to the definition of chi-square 4.1 (the non-linear dependency of chi-square on model parameters) we expect to observe a parabolic behaviour.

Figure 4.8 demonstrates chi-square vs parameters plots for the same model as 4.7.

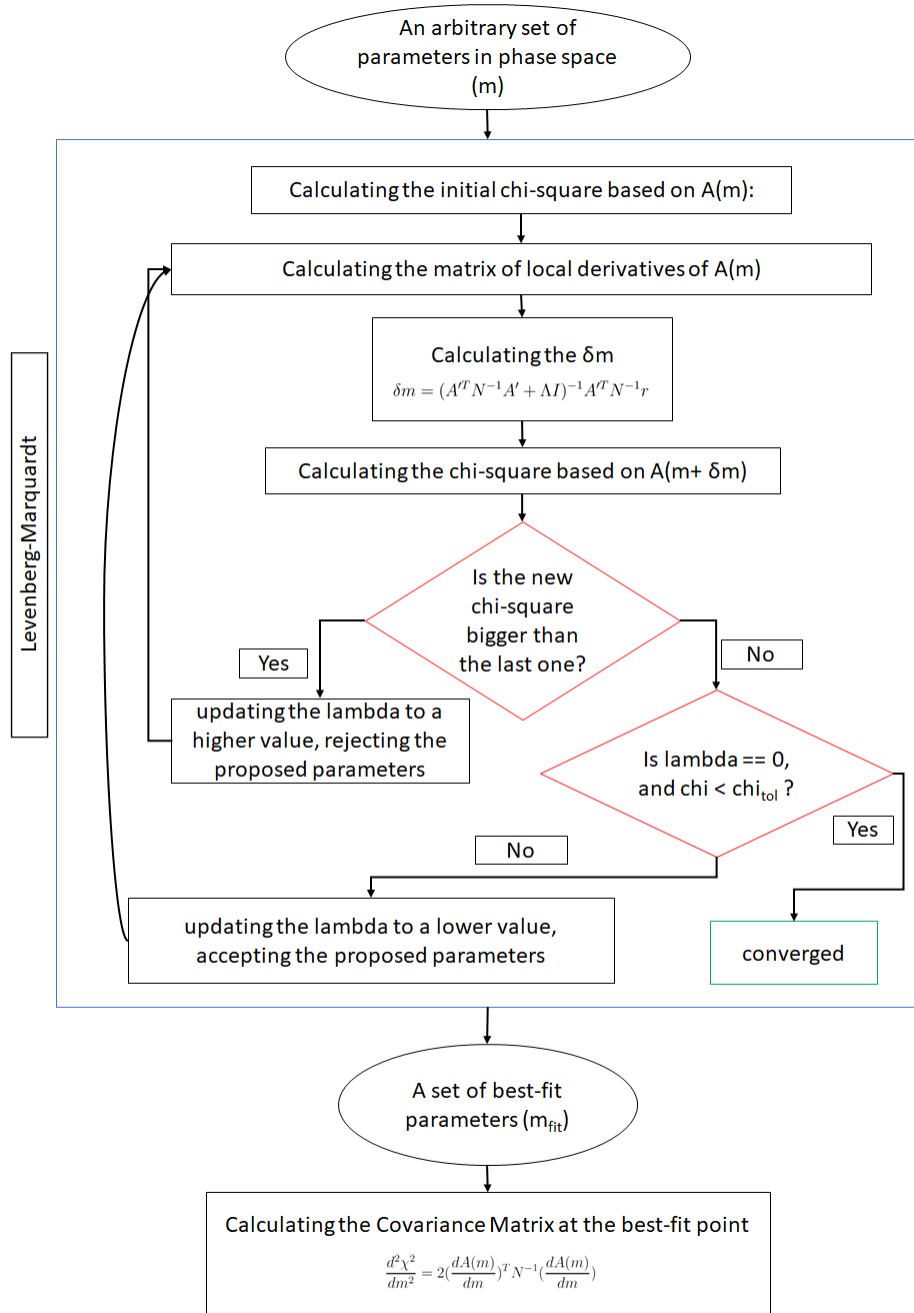


Figure 4.1: Flow chart depicting the Levenberg-Marquardt algorithm. The algorithm starts with the calculation of the χ^2 based on the theoretical model predicted by the initial set of parameters. Then, the new δm is found using 4.18 and its associated χ^2 is calculated. The new χ^2 is compared to its value from the last iteration and the value of the Λ is determined upon the success or failure of the current iteration. The algorithm is considered as converged if $\Lambda = 0$ and the χ^2 decreases less than a certain threshold amount.

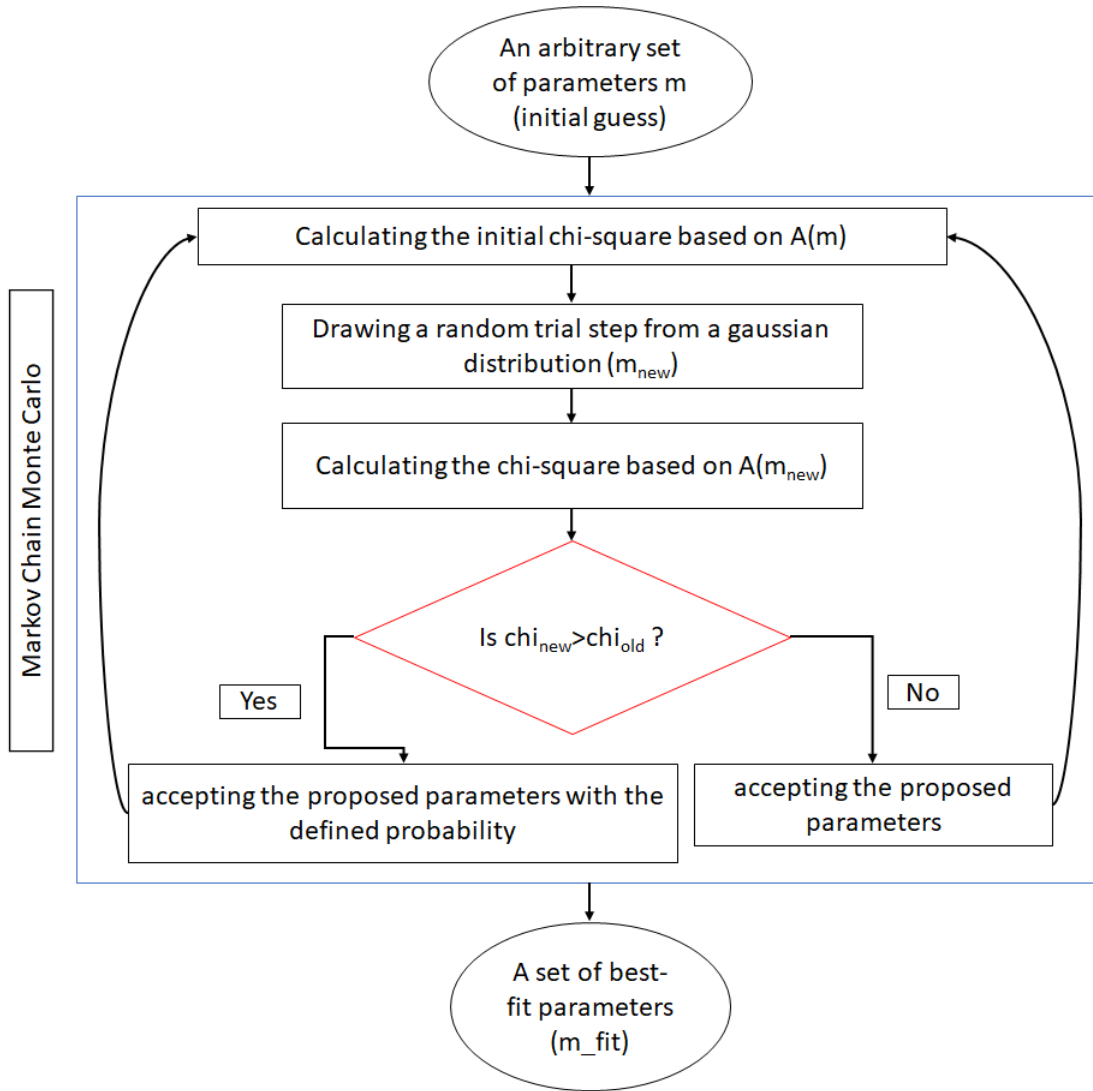


Figure 4.2: Flow chart depicting the Markov Chain Monte Carlo algorithm. The algorithm starts with the calculation of the χ^2 based on the theoretical model predicted by the initial set of parameters. Then, a new set of parameters are drawn from independent one-dimensional gaussian distributions and the associated χ^2 is calculated. The new χ^2 is compared to its value from the last iteration. If χ^2 has lowered, the new combination of parameters are accepted into the chain. Otherwise, the parameters will be accepted by the probability defined in 4.19. The algorithm itself is not capable of testing its own convergence. Therefore, one needs to seek other approaches.

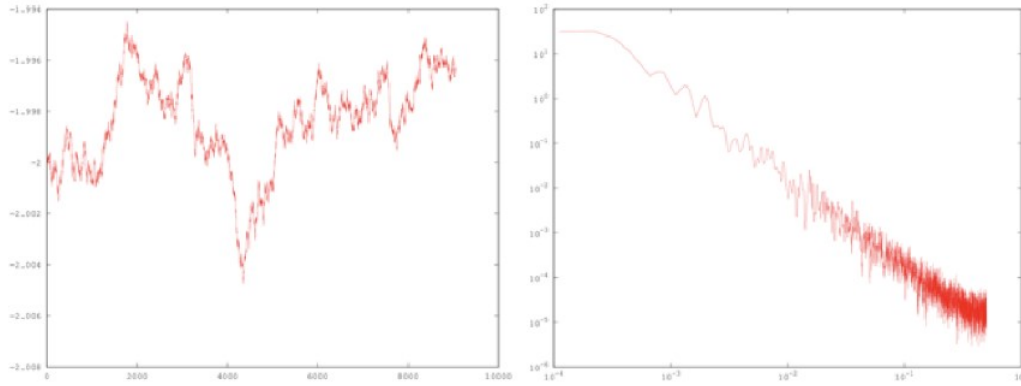


Figure 4.3: An unconverged MCMC chain (left panel) and its power spectrum (right panel): A converged MCMC chain is expected to exhibit the behaviour of a white noise. Thus, on the power spectrum, the power shall be uniformly distributed among different frequencies (after the burn-in phase of the MCMC). Here, the power tends to increase in lower frequencies, and the chain itself does not indicate the behaviour of white noise. Therefore, this chain is not yet converged. Figure from Jonathan Sievers

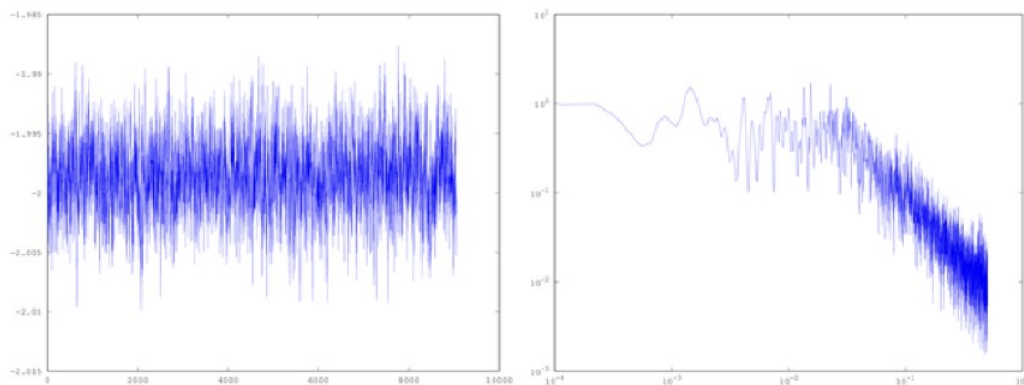


Figure 4.4: A converged MCMC chain (left panel) and its power spectrum (right panel): A converged MCMC chain is expected to exhibit the behaviour of a white noise. Thus, on the power spectrum, the power shall be uniformly distributed among different frequencies (after the burn-in phase of the MCMC). Here, the flat behaviour of the power spectrum is evident and the chain itself represents white noise. Figure from Jonathan Sievers

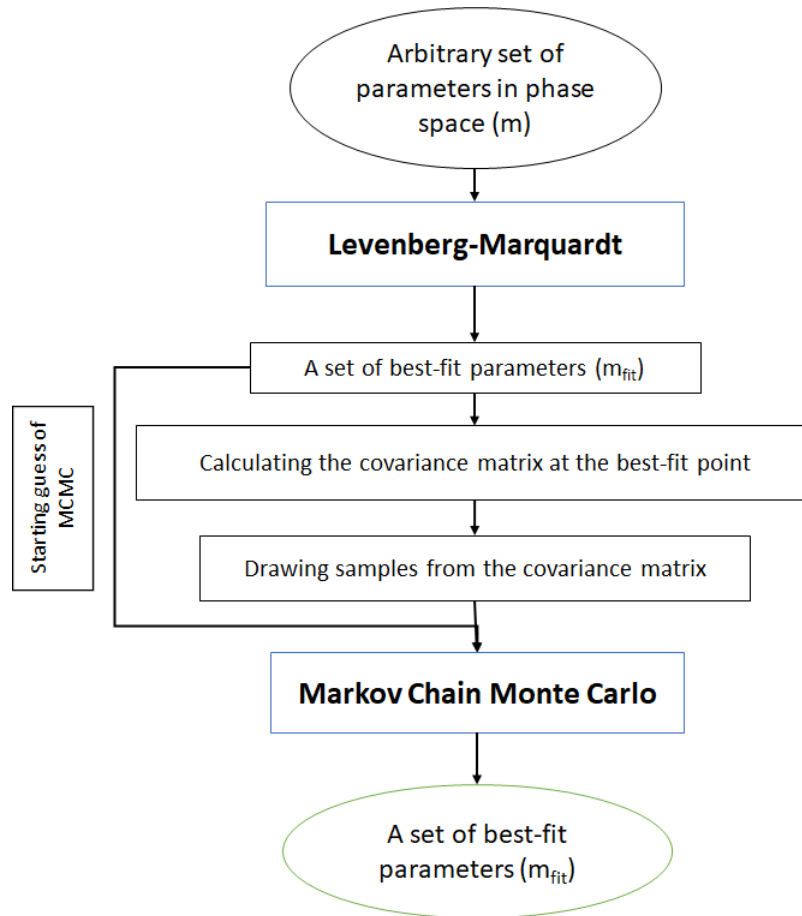


Figure 4.5: Flow chart of the procedure to combine MCMC and LM. We start by an arbitrary combination of parameters in phase space and run the LM algorithm to find the best-fit point and the covariance matrix. Then, we draw sufficient samples from the covariance matrix to use them as the posterior distribution of our MCMC. Eventually, the output of this combined method is a set of best-fit parameters and their associated error bars.

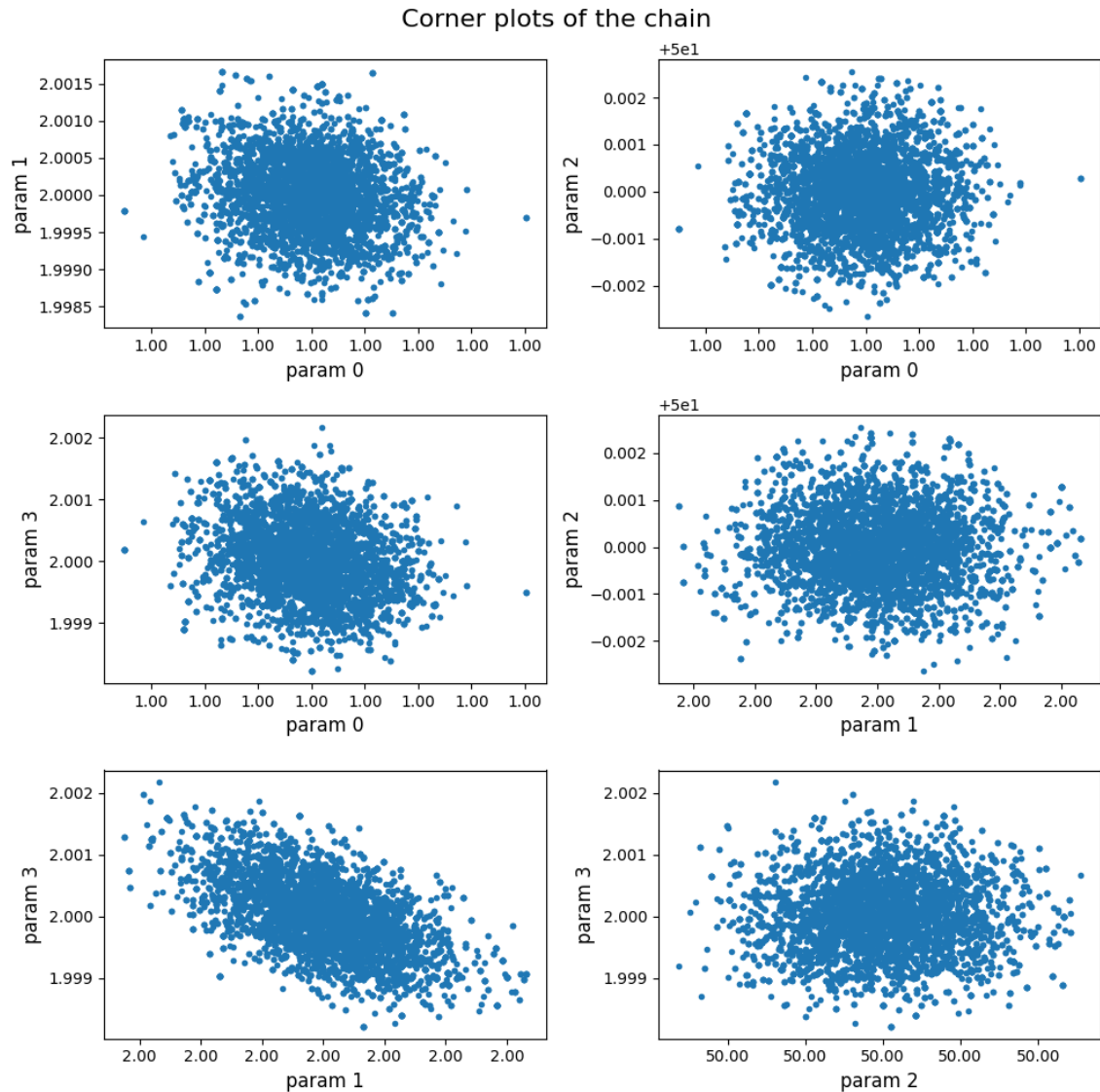


Figure 4.6: Corner plots (parameter vs parameter) of a typical MCMC chain from a four-variable Gaussian model. The lower right panel clearly shows patterns of correlation between a pair of parameters. Sampling from a multivariate normal distribution based on the covariance matrix associated with these samples will take the correlations into account.

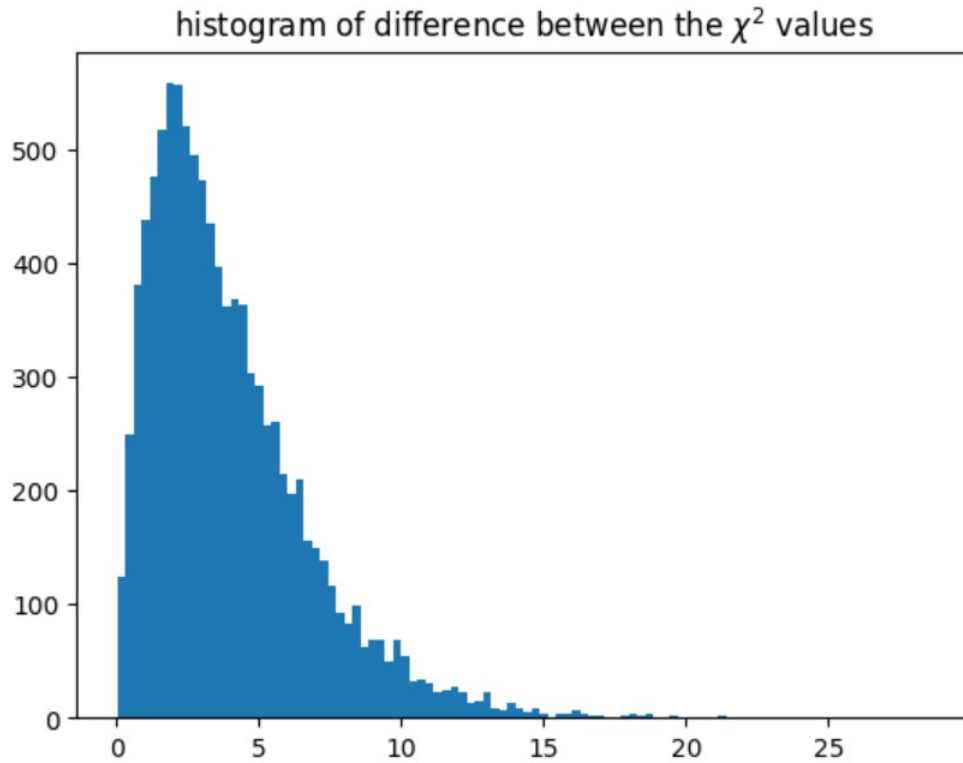


Figure 4.7: Histogram illustrating the distribution of the values of difference between the chi-squares of drawn samples for a four variable Gaussian model. The samples are drawn from the covariance matrix calculated at the point of best-fit (output of LM). We expect the average difference in the χ^2 statistics for two different samples to be of order unity per each parameter. On this plot, the average of difference is 3.97 and the standard deviation is 2.83, in acceptable agreement with our expectations. Therefore, the best-fit parameters are considered as a "good fit".

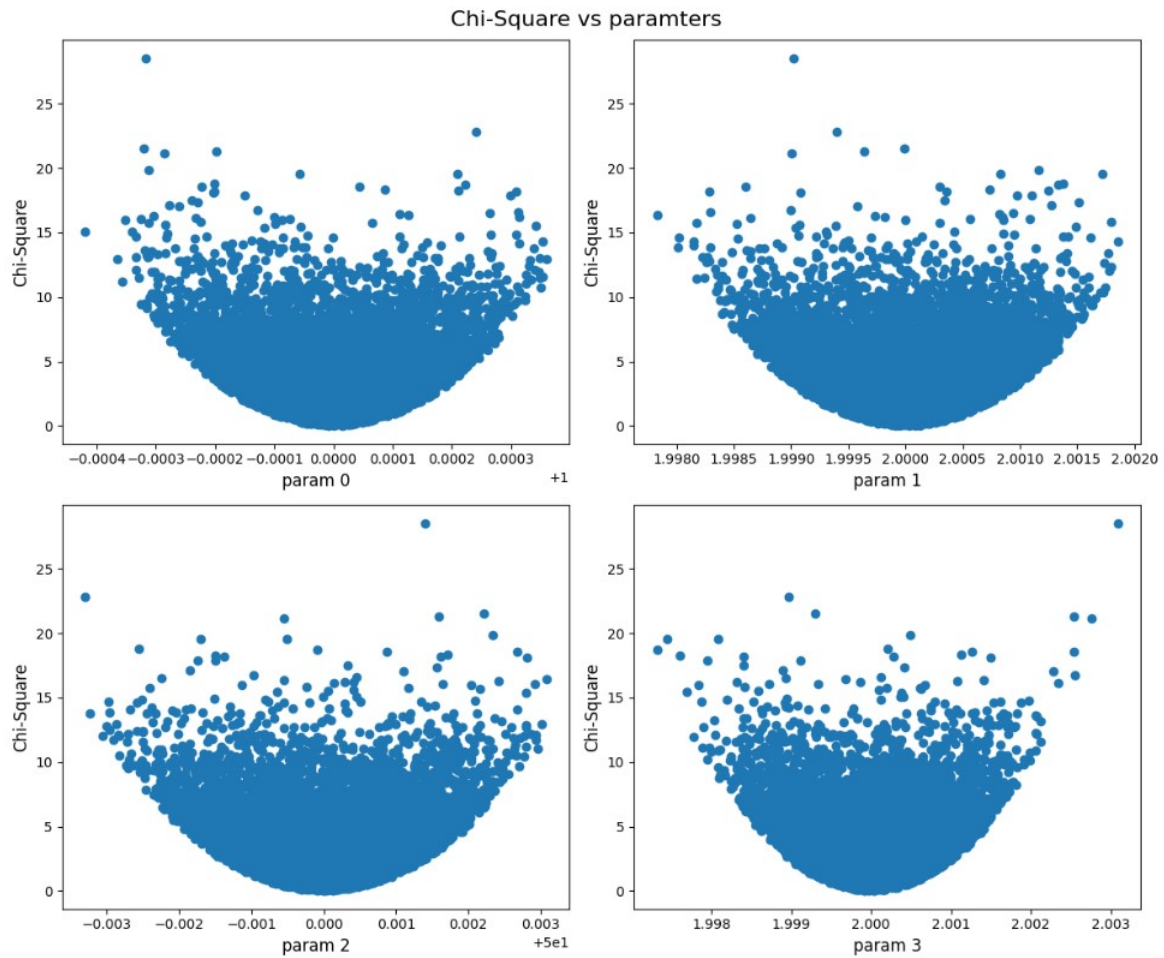


Figure 4.8: Figures demonstrating the values of chi-square associated with the drawn samples versus the values of parameters for a four variable Gaussian model. The χ^2 is expected to have a parabolic dependency on the value of parameters based on its definition (4.1). This is a test to confirm the accuracy of covariance matrix and the procedure of sample drawing.

Chapter 5

Results and Analysis

Reminder: citations for physical explanation of parameters, I guess it is better to address `pop_rad_yields` with the physical meaning, but mention that the name is different in ARES documentary.

Chapter 4 carefully described a specific method to fit an experimental data set to its corresponding theoretical model. In this chapter, we are going to impose this method to actual global 21cm curves. We chose to use ARES as our simulator to generate these curves.

5.1 Key Astrophysical Parameters in the Global 21cm Signal

According to the discussed physics of the 21cm signal in section 2.1, the shape and amplitude of this signal are intensely dependent on underlying astrophysical processes, especially those related to the star formation and reheating of the IGM. In this section, we will take the discussion further and address our current understanding of this dependency on four specific parameters which are able to effectively span the global 21cm.

By effectively constraining these parameters, significant progress can be made in comprehending the thermal history of the intergalactic medium (IGM) and the population of x-ray sources during high-redshift epochs [4].

1. f_X : High-redshift normalization factor in the relation between X-ray luminosity and SFR

X-ray photons generated by galaxies and quasars are likely the most important cause of heating the IGM. Considering the fact that the nature of high-redshift objects are not very well identified, it is not possible to give an exact theory for the high-redshift X-ray background. The safest course of action is to assume that the correlation between X-ray luminosity and SFR in high redshift is only an extrapolation of its local format.

$$L_X = 3.4 \times 10^{40} f_X \left(\frac{SFR}{1 M_\odot \text{ yr}^{-1}} \right) \text{ erg s}^{-1} \quad (5.1)$$

Where f_X is an unknown normalization factor at high redshift and is believed to evolve by redshift. The normalization was chosen so that, with $f_X = 1$, the total X-ray luminosity per unit SFR is consistent with that observed in starburst galaxies at the present epoch [4, 5].

2. N_{lw} : Number of photons emitted in the Lyman-Werner band ($11.2 - 13.6\text{eV}$) per baryon of star formation (This parameter is referred to as *pop_rad_yield_0_* in ARES documentation), cite ARES documentation
 3. N_{ion} : Mean number of ionizing photons produced per baryon of star formation (This parameter is referred to as *pop_rad_yield_2_* in ARES documentation)
 4. f_{esc} : Fraction of ionizing photons that escape their host galaxy into the IGM
- f_{esc} and N_{ion} are both defined in the process of calculating the evolution of ionization fraction \bar{x}_i :

$$\bar{x}_i = \frac{\zeta f_{coll}}{1 + \bar{n}_{rec}} \quad (5.2)$$

$$f_{coll} = \int_{m_{min}}^{\infty} dm m n(m) \quad (5.3)$$

$$\zeta = A_{He} f_* f_{esc} N_{ion} \quad (5.4)$$

f_{coll} is the collapse fraction (fraction of gas inside collapsed objects, fraction of mass in halos more massive than m_{min}), \bar{n}_{rec} is the mean number of recombinations per ionized

hydrogen atom, ζ is the ionizing efficiency, f_* is the star formation efficiency (fraction of baryons converted into stars), and $A_{He} = 4/(4 - 3Y_p) = 1.22$, where Y_p is the mass fraction of helium, is a correction factor to convert the number of ionizing photons per baryon in stars to the fraction of ionized hydrogen. Our limited understanding of the mass distribution of the emitting stars introduces an uncertainty in the number of ionizing photons per baryon N_{ion} that is emitted by galaxies. There is also considerable uncertainty in the fraction of ionizing photons f_{esc} that escape the host galaxy to ionize the IGM. That's why we chose these parameters. Observations will help to constrain them.

These parameters enter our model as a factor multiplying the SFR and are, therefore, individually degenerate with the star-formation efficiency f_* . That's why we did not choose to use f_* [4, 5].

Figure 5.1 shows the effect of changing these parameters on an actual 21cm curve.

We take the above-mentioned physical parameters as fitting parameters and we try to find their best-fit values and corresponding error-bars.

5.2 Parameter Estimation of an ARES generated curve

Before using our developed script to fit actual data, we use it to fit a known ARES curve as a verification test. We generate an ARES curve with a fixed set of parameters and we

use these curve as the imaginary "data". If the algorithm returns the same parameter values (with in the error-bar range), we can make sure that it is working correctly.

We begin by using the LM and we find inverse of covariance matrix for our chosen combination of parameters, which we will later use to generate our correlated samples.

Parameters:

$$pop_rad_yield_0 : 10^4, \quad pop_rad_yield_2 : 10^3, \quad f_{esc} : 0.1, \quad f_X : 0.1 \quad (5.5)$$

Inverse of covariance matrix for this set of parameters:

$$\begin{pmatrix} 1.64 \times 10^{-3} & 1.96 \times 10^{-2} & -4.39 \times 10^{-7} & -5.37 \times 10^{-8} \\ 1.96 \times 10^{-2} & 1.60 \times 10^1 & -1.44 \times 10^{-3} & -5.94 \times 10^{-6} \\ -4.39 \times 10^{-7} & -1.44 \times 10^{-3} & 1.38 \times 10^{-7} & 2.15 \times 10^{-10} \\ -5.37 \times 10^{-8} & -5.94 \times 10^{-6} & 2.15 \times 10^{-10} & 1.38 \times 10^{-11} \end{pmatrix} \quad (5.6)$$

Now, we are prepared to draws our samples based on method described in 4.3.1. Figure 5.10 illustrates the distribution of samples for the above-mentioned four parameters. As a sanity check, we calculate the mean and standard deviation of these distribution. We expect the mean to be close to values of 5.5. Table 5.1 represents the values of mean and standard deviation, which is in agreement with the expectations.

In section 4.4, we introduced two methods to check the algorithm and the quality of fit.

Parameter \ Value	$pop_rad_yield_0_$	$pop_rad_yield_2_$	f_{esc}	f_X
Mean	9.99999993×10^3	1.00002933×10^3	9.99962873×10^2	1.00000029×10^1
Standard Deviation	4.08174690×10^2	4.03138658×10^0	3.74407952×10^4	3.72581029×10^6

Table 5.1: Mean and standard deviation of samples drawn from the covariance matrix 5.6

Performing the chi-square test on our samples showed that the average difference between the chi-square of drawn samples is 49.20, which we expected to be 4. Although it is approximately one order of magnitude bigger than the expectations, it can be still considered a good fit.

We proceed by performing the second test, which is plotting the values of chi-square of samples versus the parameter values. The results are shown in 5.11. In the hypothetical ideal case, We expected to see a parabolic behaviour. Figure 5.5 shows the zoomed version of results. We can infer a parabolic behaviour in low values of chi-square.

Now that we have our samples, we proceed to run the MCMC chain with them. The overall results of the fit and the final resulting curve are shown in 5.4 and ?? respectively. Figure 5.13 indicates the white-noise behaviour of parameters throughout the chain which is consistent with our anticipation for a converged chain. We confirm the convergence by looking at the power spectrum in Figure 5.14. Flat behaviour in low frequencies is apparent.

It is worth mentioning that the method described in chapter 4 and used in this section, is flexible to the change of parameters of the model (which in our case, is ARES.¹). However, these parameters are only physically meaningful in a limited region of phase

¹List of parameters can be found in ARES documentation.

Parameter Value	$pop_rad_yield_0_$	$pop_rad_yield_2_$	f_{esc}	f_X
True values	1×10^4	1×10^3	0.1	0.1
Fitted values	9.99998275×10^3	9.99419824×10^2	$1.00025031 \times 10^{-1}$	$1.00001169 \times 10^{-1}$
Error-bar of fit	$3.54171104 \times 10^{-2}$	3.86126208×10^0	$3.57822431 \times 10^{-4}$	$3.39295495 \times 10^{-6}$
Fitting Error	0.00013093%	0.02645403 %	0.01527014%	0.00032365%

Table 5.2: Results of fitting a known ARES curve with MCMC chain

space (A hypercube where the combination of parameters are physically meaningful).

Going beyond this region will result in a failure in calculating the global 21cm curve. our

developed script is designed to handle this issue and stop it from aborting the whole run ²,

but the MCMC might not be able to reach convergence if the algorithm faces a lot of

samples beyond the allowed region.

5.3 Parameter estimates of EDGES data and uncertainties

5.3.1 Choice of "multiplication factor"

5.3.2 error bar calculation

Reminder: not exactly sure where this equation comes from

We need to know the error bar of the observational data (EDGES) to run the MCMC

²The python code for the MCMC is designed such that it will return an arbitrary large chi-square for those combination of parameters which ARES is unable to handle. Therefore, the probability of these points getting accepted into the chain will be systematically low.

chain. These error bars are usually taken from the noise model. In order to make our life easy, instead of dealing with the EDGES noise model which is hard and messy, we use the following straight forward equation which comes from the radiometer equation:

$$\frac{\delta T}{T_{sys}} = \frac{1}{\sqrt{Bt}} \quad (5.7)$$

Where B is the bandwidth, t is the exposure time and T_{sys} is the system temperature. Assuming the bandwidth of 10^6 , exposure time of one day and and temperature of 3000K, we get: $\delta T = 10^{-2}K = 10mK$

5.3.3 results

We proceed by doing the same procedure as section 5.2. However, this time we use the EDGES data (with half of the actual amplitude) as our observational data in MCMC. This half amplitude is chosen using the insights from section ?? . One of the main issues is that since the shape of the EDGES data is not very close to the predicted theoretical curve, the resulting fit is not very perfect. We first run the LM to find the covariance matrix and

Parameter Value	$pop_rad_yield_0_$	$pop_rad_yield_2_$	f_{esc}	f_X
Mean	4.54933238×10^3	2.47654876×10^3	$3.70006283 \times 10^{-1}$	$1.36397845 \times 10^{-1}$
Standard Deviation	$1.81616137 \times 10^{-1}$	1.56788160×10^2	$2.34431702 \times 10^{-2}$	$6.32705006 \times 10^{-6}$

Table 5.3: Mean and standard deviation of samples drawn from the covariance matrix 5.8

Parameter Value	$pop_rad_yield_0_$	$pop_rad_yield_2_$	f_{esc}	f_X
Fitted values	9.999×10^3	9.994×10^2	1.000×10^{-1}	1.000×10^{-1}
Error-bar of fit	3.541×10^{-2}	3.861×10^0	3.578×10^{-4}	3.392×10^{-6}

Table 5.4: Results of fitting EDGES data with MCMC chain

generate our samples.

$$\begin{pmatrix} 3.24 \times 10^4 & 5.68 \times 10^6 & -8.51 \times 10^2 & 5.65 \times 10^{-1} \\ 5.68 \times 10^6 & 2.43 \times 10^{10} & -3.63 \times 10^6 & 5.64 \times 10^0 \\ -8.51 \times 10^2 & -3.63 \times 10^6 & 5.44 \times 10^2 & -9.80 \times 10^{-4} \\ 5.65 \times 10^{-1} & 5.64 \times 10^{00} & -9.80 \times 10^{-4} & 3.92 \times 10^{-5} \end{pmatrix} \quad (5.8)$$

We again run the MCMC from the drawn samples. The results are shown in table 5.4. Figure 5.15 and 5.16 present the trend of values of chi-square throughout the chain and corner plots of parameters. Figure 5.15 and 5.16 present the trend of values of chi-square throughout the chain and corner plots of parameters.

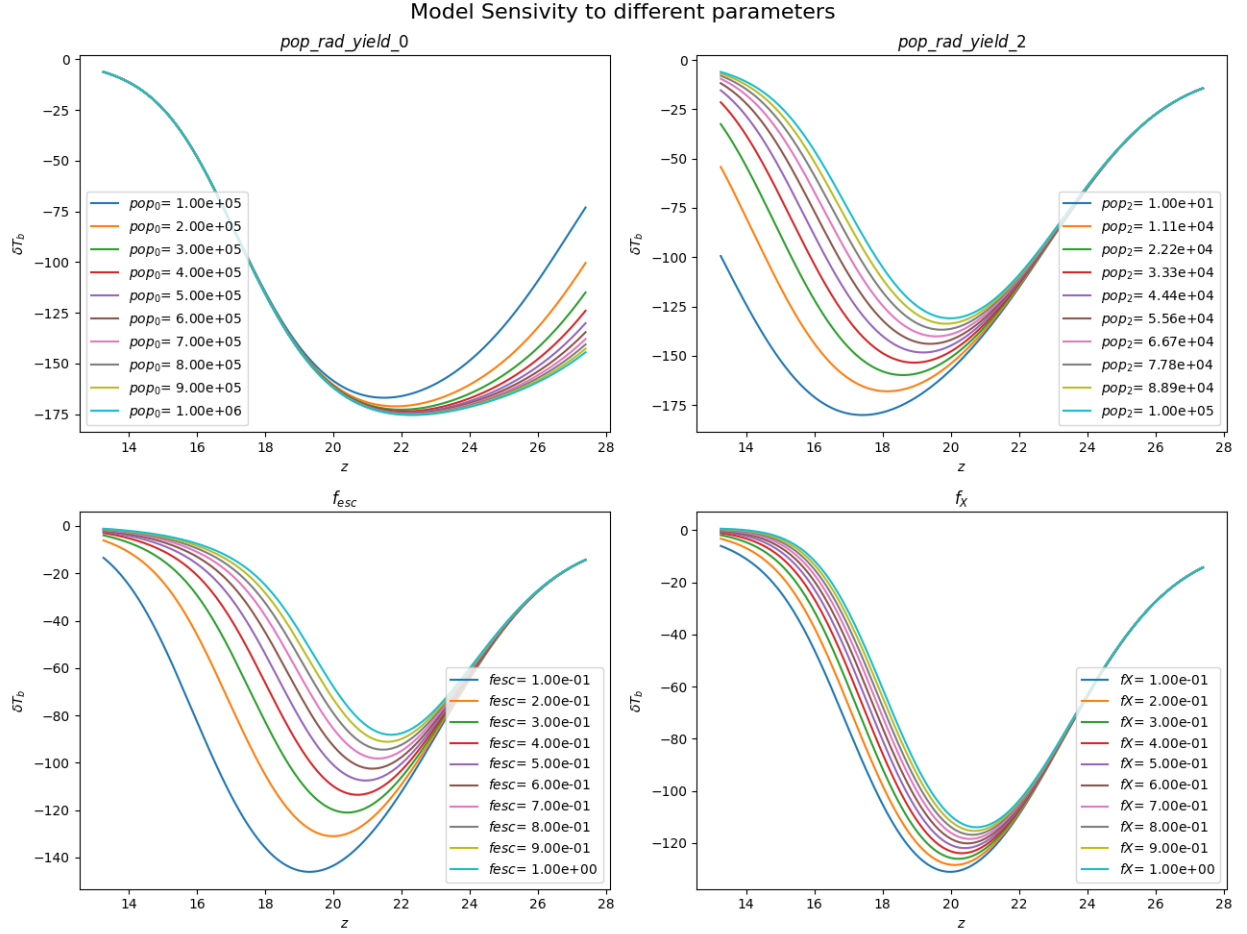


Figure 5.1: Behaviour of ARES-generated global 21cm models with respect to four parameters: $pop_rad_yield_0$, $pop_rad_yield_2$, f_{esc} , and f_X . In each panel, the corresponding parameter possesses 10 different values and all other parameters are kept at default values by ARES

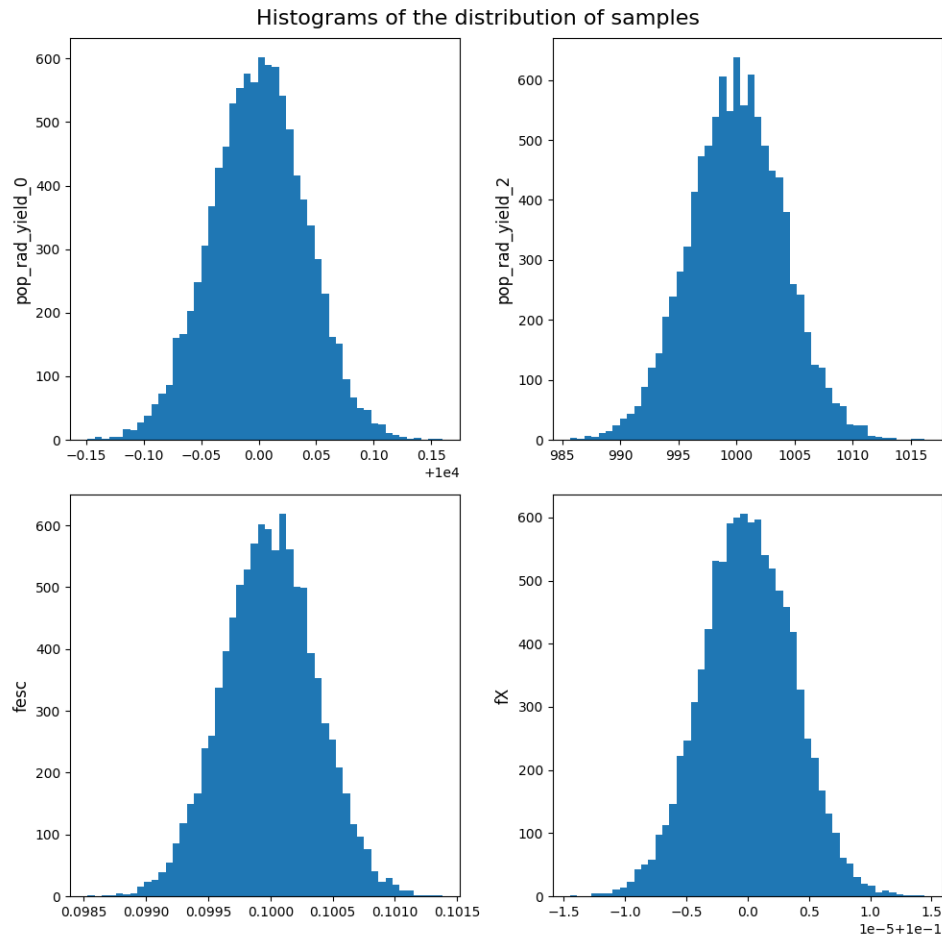


Figure 5.2: Histogram of distribution of samples before feeding to MCMC, The mean of these distributions are consistent with values given in 5.5.

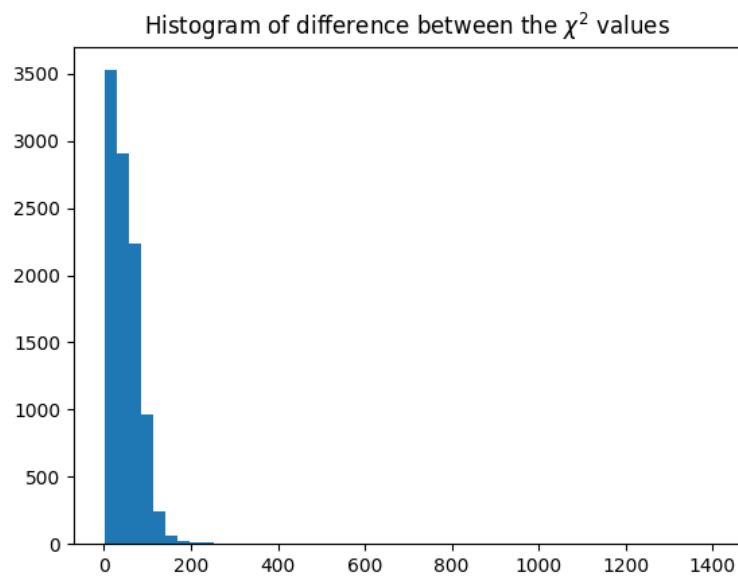


Figure 5.3: Histogram of Chi-Square of drawn samples, the mean is 49.20 with standard deviation of 41.98.

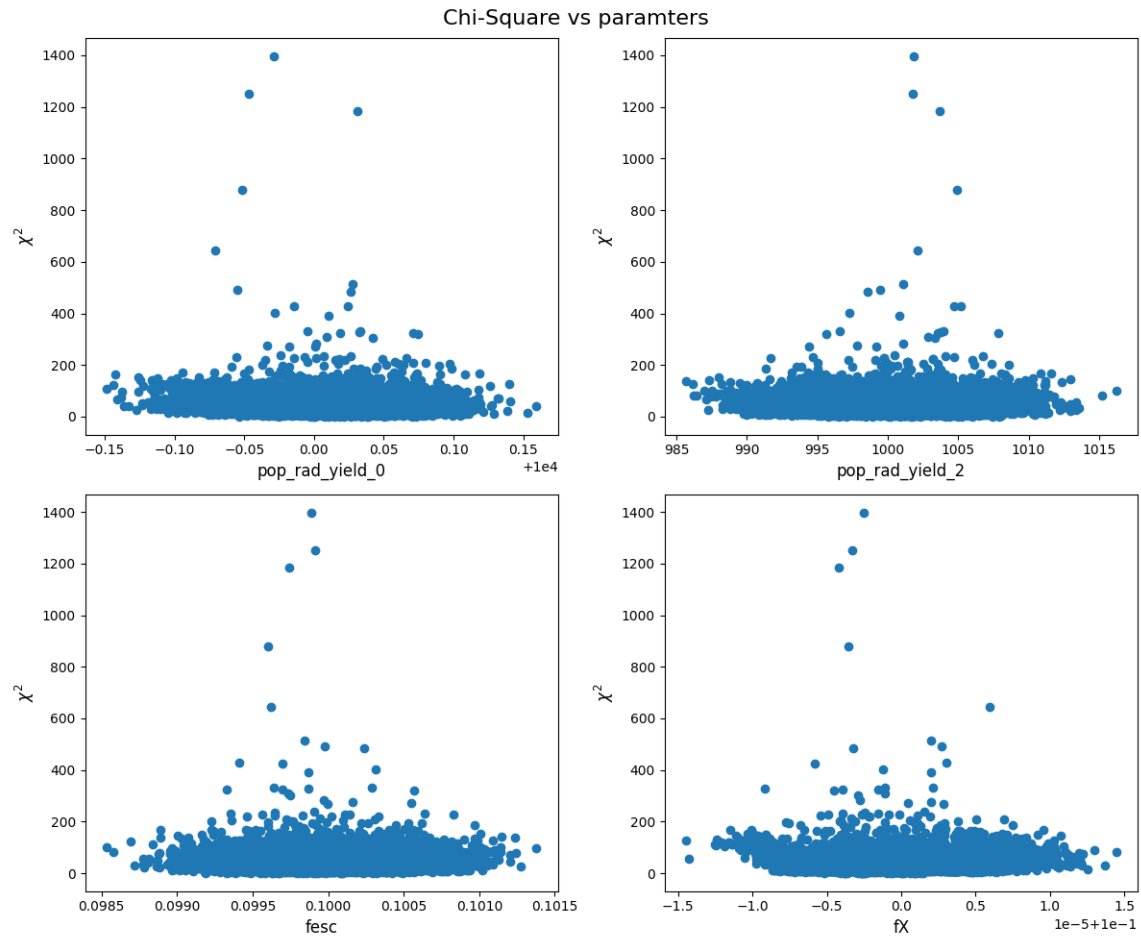


Figure 5.4: Chi-Square of Drawn samples versus parameter values for a known ARES curve with four parameters, The parabolic behaviour is not obvious in these plots.

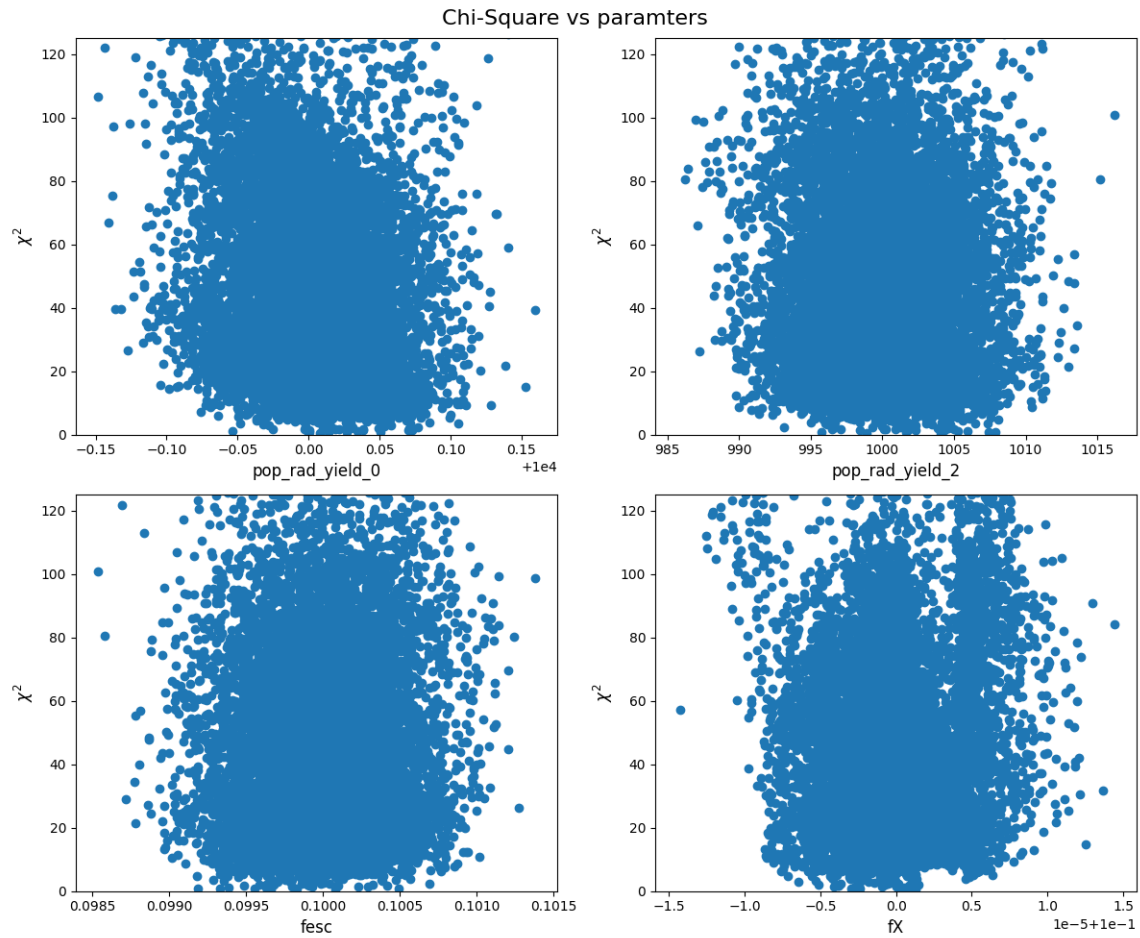


Figure 5.5: Zoomed version of figure 5.12, A weak parabolic behaviour is observed for low values of χ^2 .

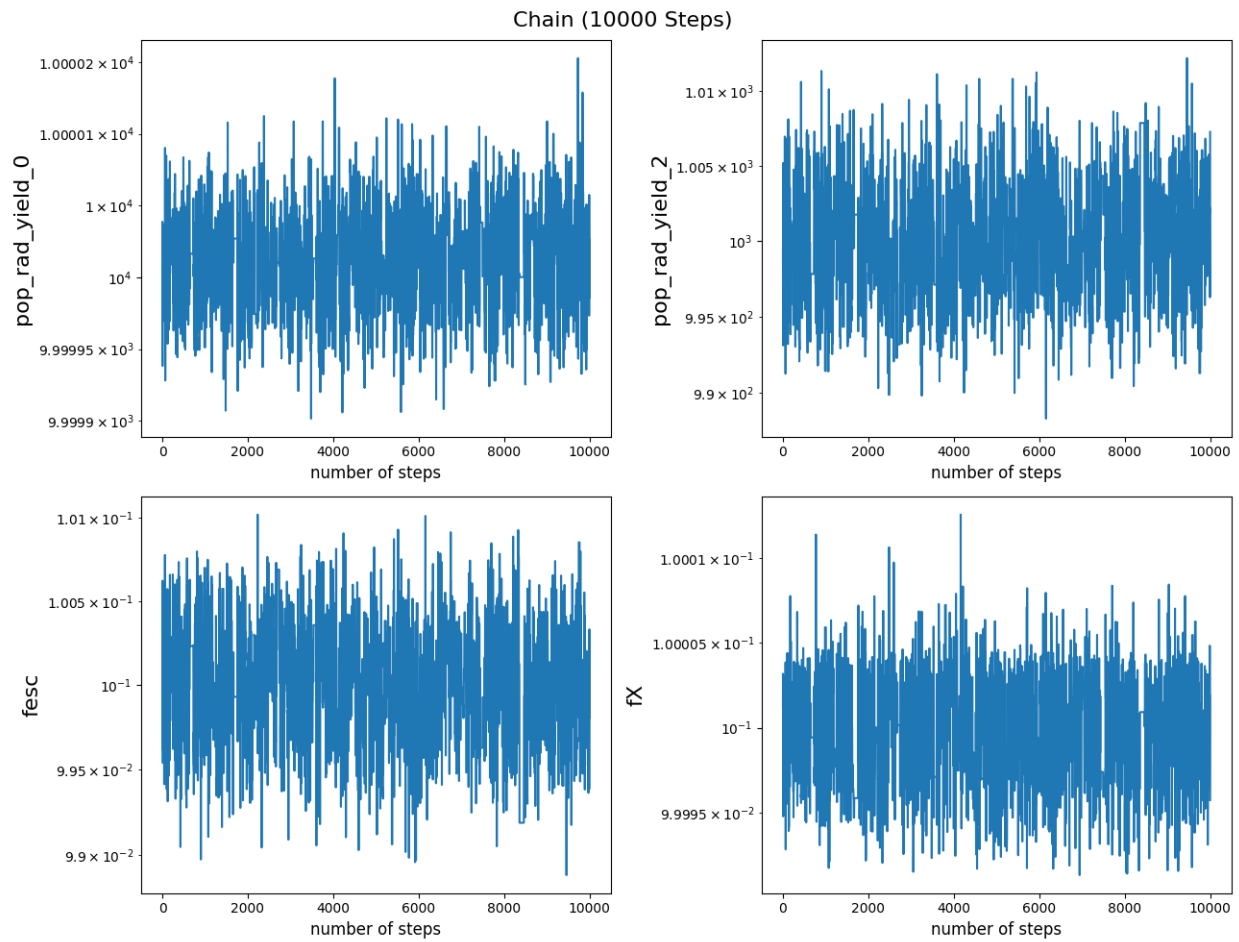


Figure 5.6: Trend of parameters in the MCMC chain, White noise behaviour is considered as a sign of convergence. The acceptance ratio of the chain is 22.12%.

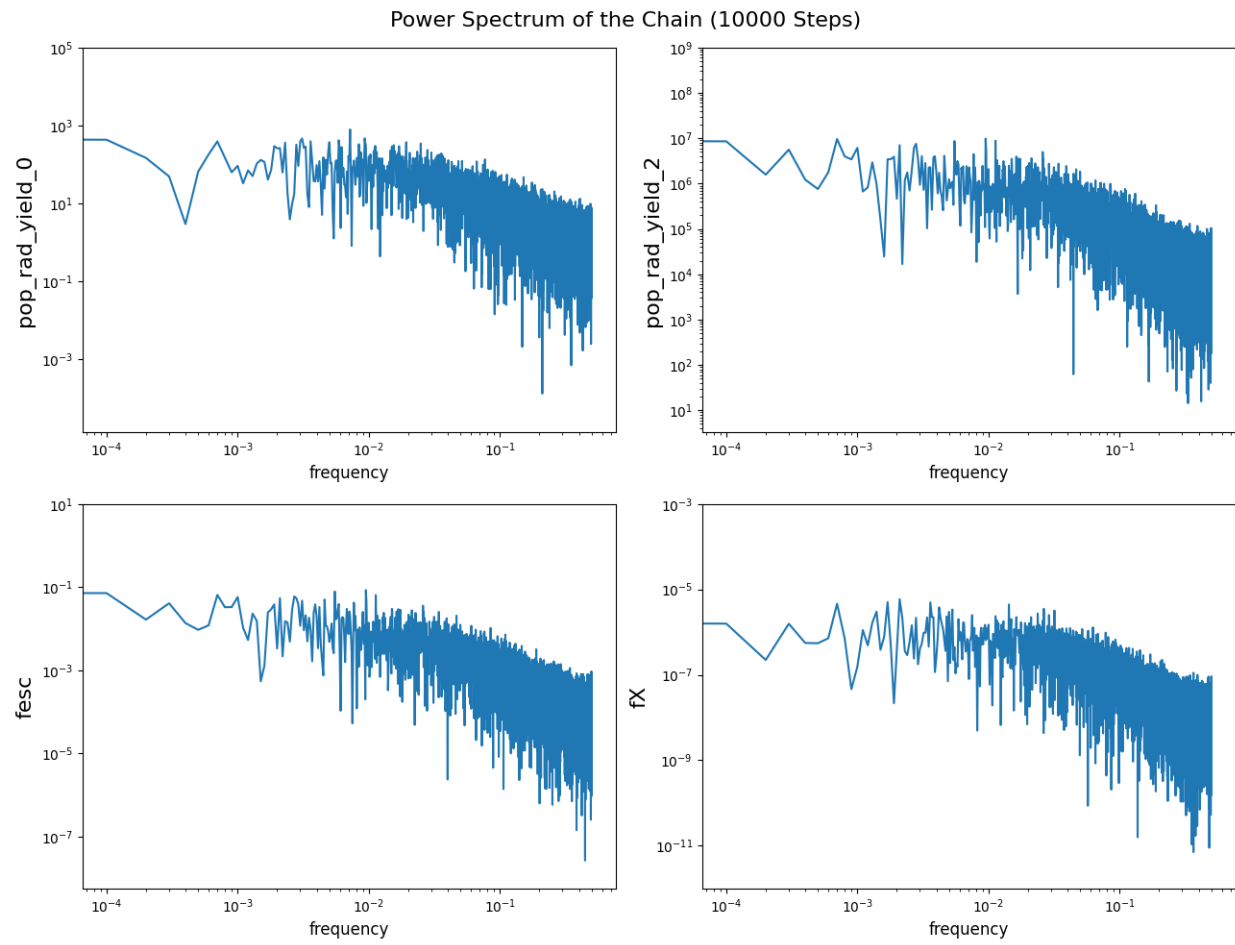


Figure 5.7: Power spectrum of the chain, Flat behaviour in low frequencies is in agreement with results of 5.13.

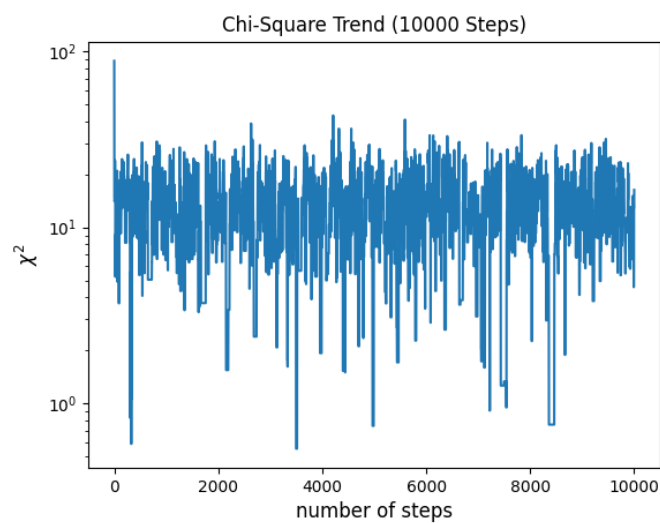


Figure 5.8: Trend of chi-square in the MCMC chain, The chain seems to have reached an equilibrium state.

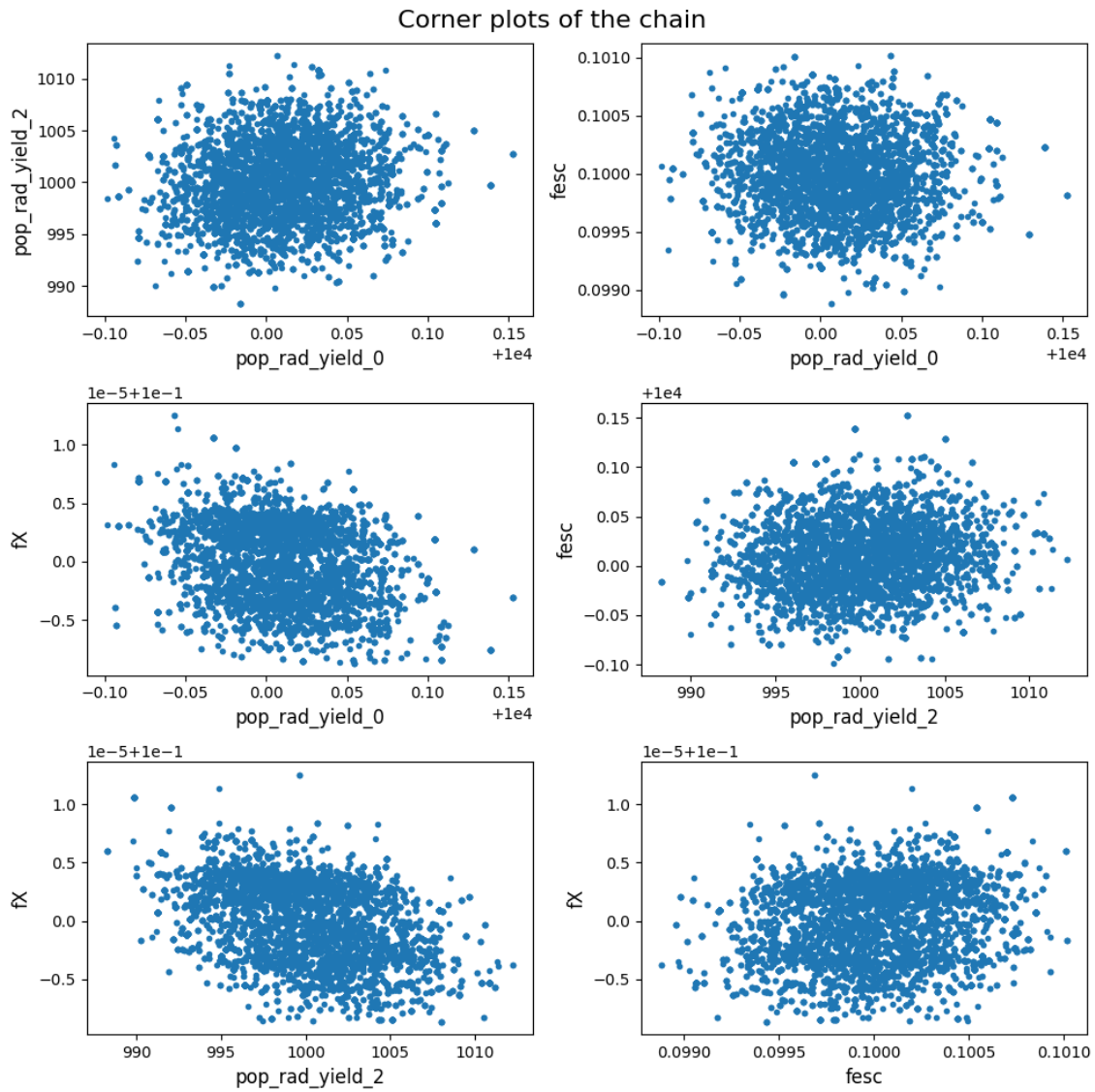


Figure 5.9: Corner plots of the chain indicating the correlation between the parameters specially in the lower left panel

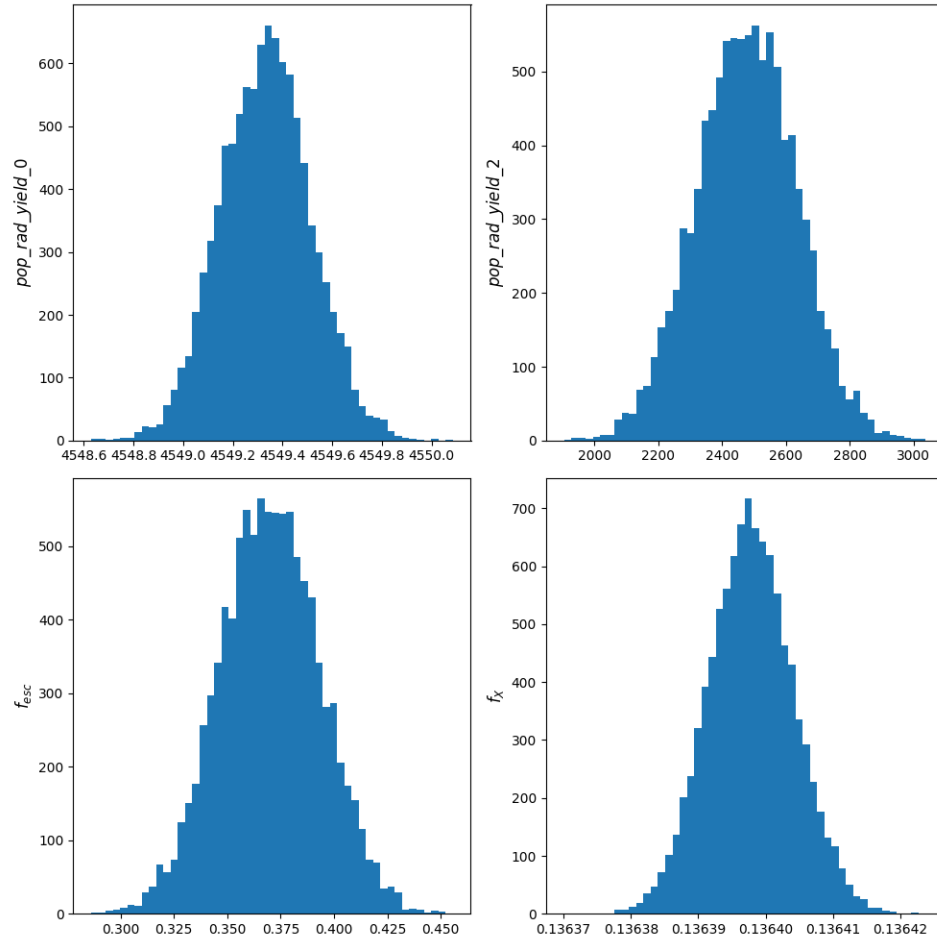


Figure 5.10: Histogram of distribution of samples before feeding to MCMC, The mean of these distributions are consistent with values given in 5.5.

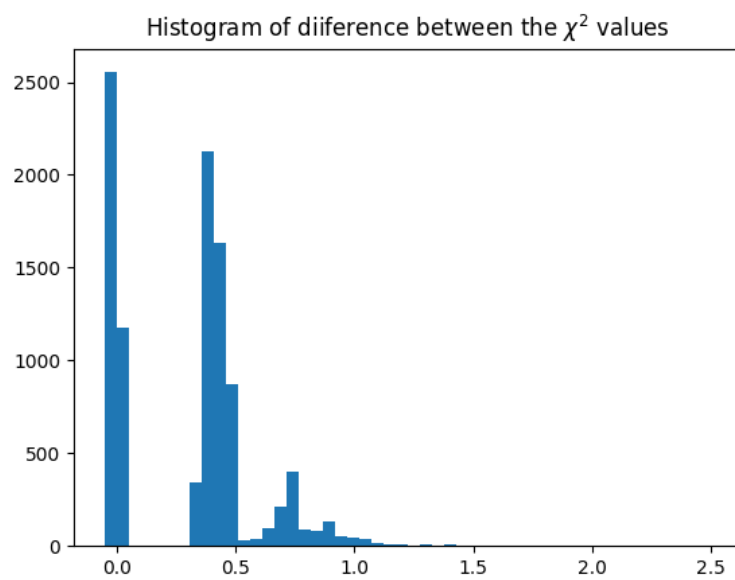


Figure 5.11: Histogram of Chi-Square of drawn samples, the mean is 49.20 with standard deviation of 41.98.

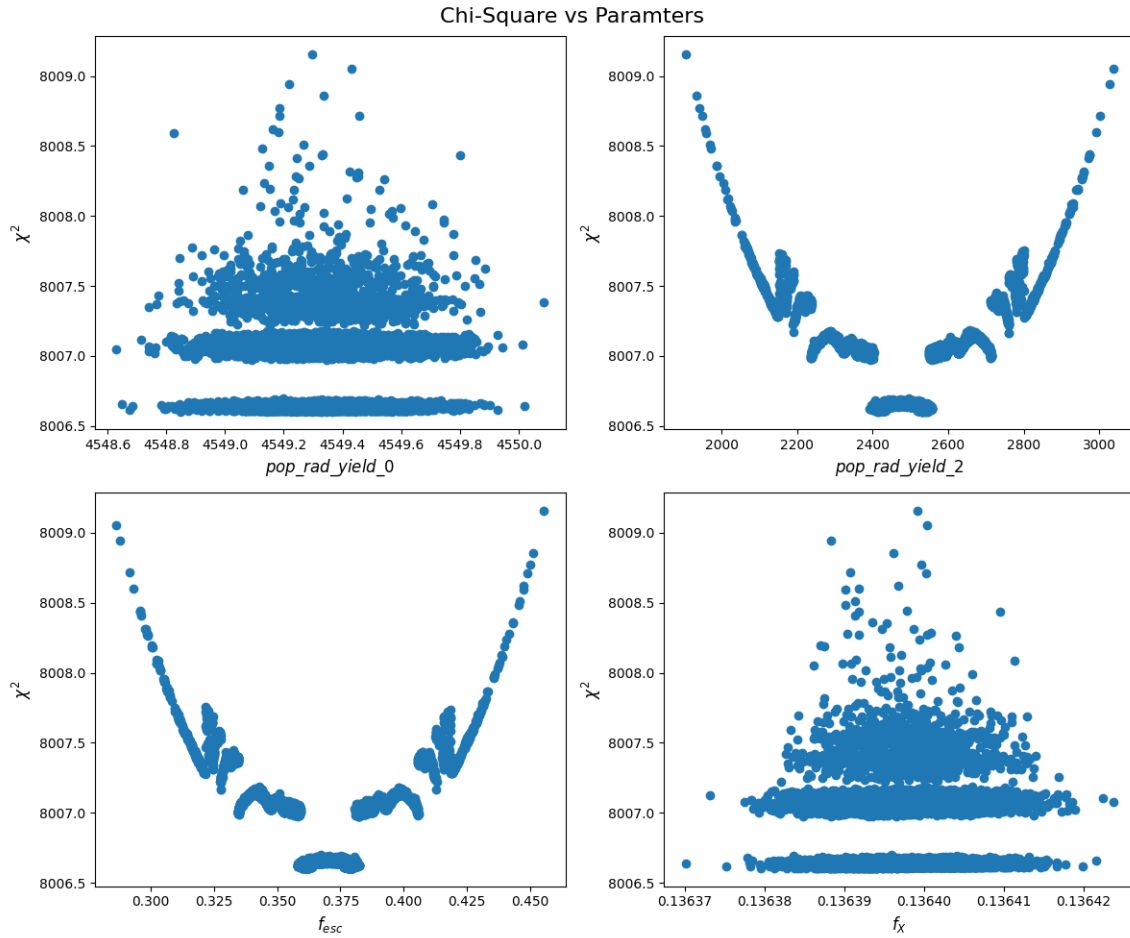


Figure 5.12: Chi-Square of Drawn samples versus parameter values for a known ARES curve with four parameters, The parabolic behaviour is not obvious in these plots.

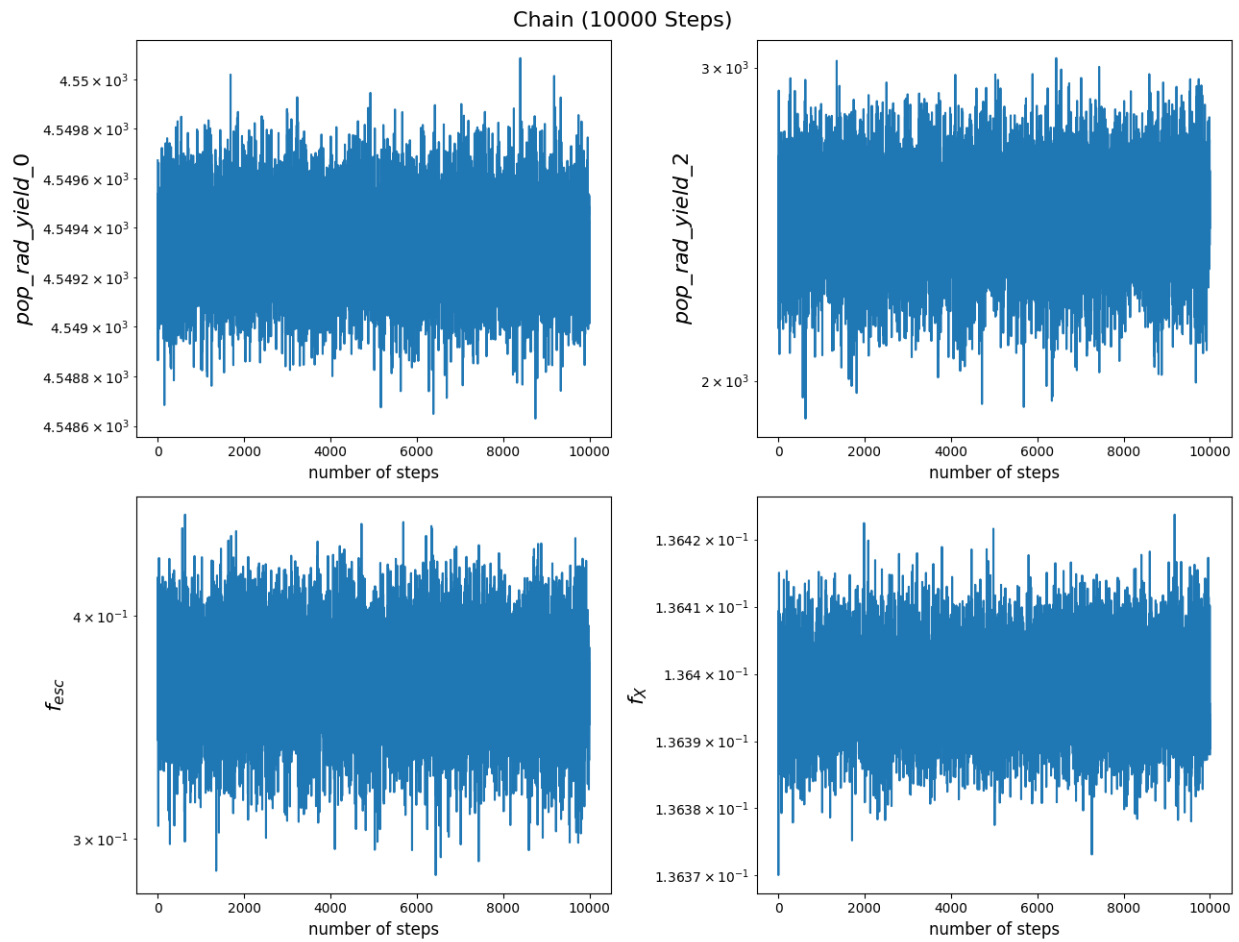


Figure 5.13: Trend of parameters in the MCMC chain, White noise behaviour is considered as a sign of convergence. The acceptance ratio of the chain is 22.12%.

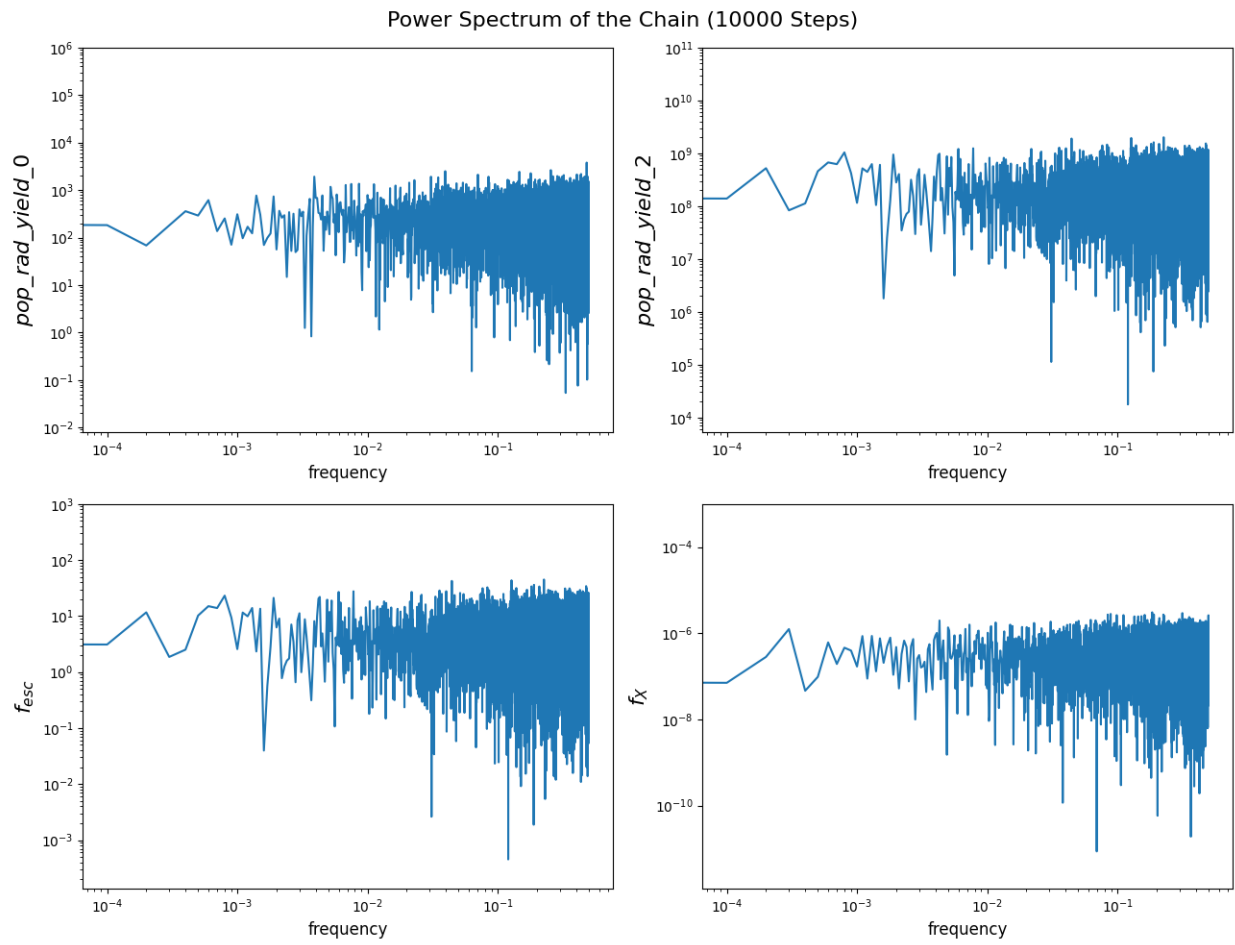


Figure 5.14: Power spectrum of the chain, Flat behaviour in low frequencies is in agreement with results of 5.13.

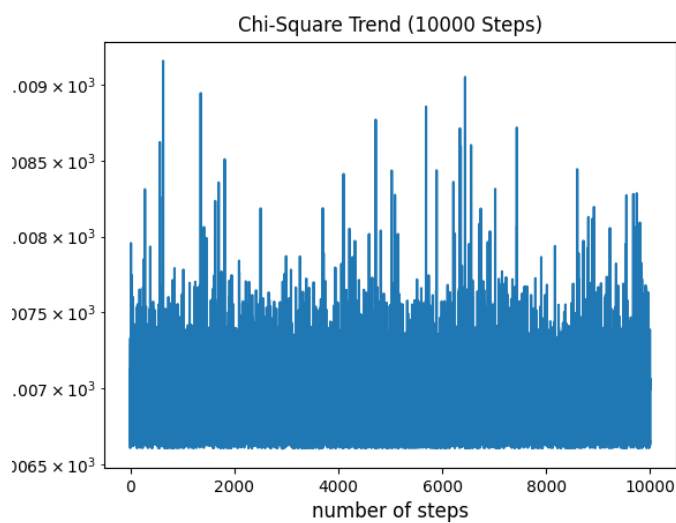


Figure 5.15: Trend of chi-square in the MCMC chain, The chain seems to have reached an equilibrium state.

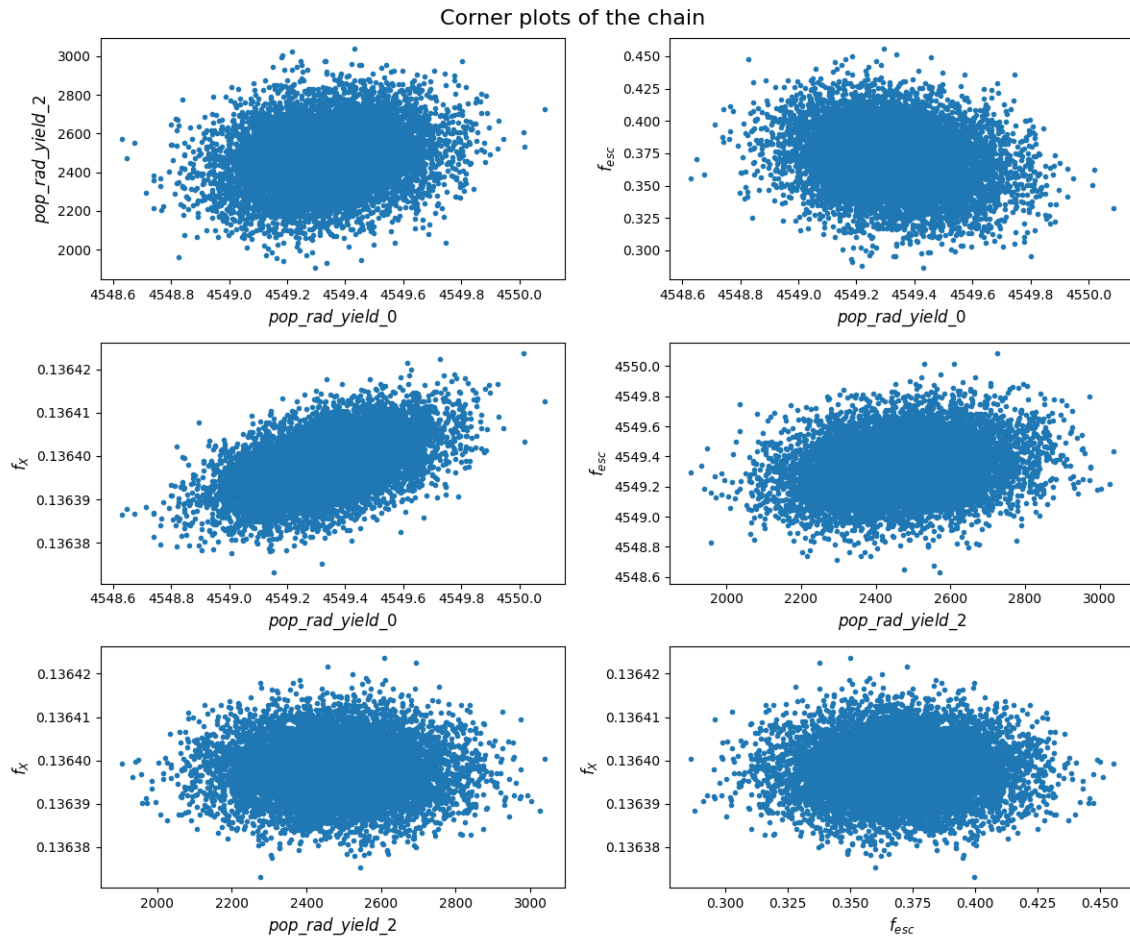


Figure 5.16: Corner plots of the chain indicating the correlation between the parameters specially in the lower left panel

Chapter 6

Discussion and Conclusion

6.1 Interpretation of the results

6.2 Summary of the main findings

6.3 Comparison with previous studies and observations

6.4 Contributions and significance of the research

6.5 Limitations

We faced certain limitation while working on this research. Most of those emerged during the implementation of python script. An strongly limiting obstacle is related to the ARES's

run time which is in the order of a few seconds per each simulation (approximately 4 to 5 seconds for different combination of parameters). Given that ARES is computationally heavy, it will make it hard to use algorithms based on using ARES on each iteration ¹. This was main the reason that led us to combine the MCMC with LM in order to have a more efficient chain and guarantee the convergence.

6.6 Future work

As the first step, the developed script is going to be published as a python package in near future. There will be a corresponding paper describing a summary of the results shown in chapter 5.

We plan to take the analysis further and include a realistic foreground model. Then, we will add some of the previously mentioned non-standard effects to ARES simulations and run the same described method to observe the difference the best-fit curve. The results will hopefully tell us if existing and future observational data (like EDGES) is a sign of new physics and can be explained through physics beyond standard cosmological model.

¹As an example, the run time for the MCMC results presented in chapter 5 was approximately 13 hours.

Chapter 7

Appendices

7.1 Derivation of radiometer equation

7.2 Code snippets and scripts

7.2.1 Levenberg-Marquardt

7.2.2 Markov Chain Monte Carlo

7.2.3 drawing samples from covariance matrix

Listing 7.1: Python example

```
def draw_samples(covariance_matrix , nset):
```

"""

covariance_matrix: covariance matrix

nset: the number of samples

returns: a matrix of samples

*This function calculates a series of correlated samples based on the pres
covariance matrix and the number of samples.*

*The shape of the output is (nset, m) where m comes from the shape of
covariance matrix and it typically shows the number of parameters in the*

"""

#normalizing the covariance matrix

`D = np.diag(np.diag(covariance_matrix))` *#diagonal matrix of covariance m*

`D_sqrt = np.sqrt(D)`

`D_inv_sqrt = np.linalg.pinv(D_sqrt)`

#normalized covariance matrix

`covariance_matrix_normalized = D_inv_sqrt @ covariance_matrix @ D_inv_sqrt`

`e, v = np.linalg.eigh(covariance_matrix_normalized)`

`e[e<0]=0` *#omitting any negative eigenvalues due to roundoff*

`n = len(e)`

```
#make gaussian random variables

g=np.random.randn(n, nset)


#scaling by the square root of the eigenvalues

rte=np.sqrt(e)

for i in range(nset):

    g[:,i]=g[:,i]*rte


#calculating the samples

samples = (v@g).T

#denormalizing the samples

samples_denormalized = samples @ D_sqrt

return samples_denormalized
```


Bibliography

- [1] C. Carilli, S. Furlanetto, F. Briggs, M. Jarvis, S. Rawlings, and H. Falcke, “Probing the dark ages with the square kilometer array,” *New Astronomy Reviews*, vol. 48, no. 11, pp. 1029–1038, 2004. Science with the Square Kilometre Array.
- [2] S. G. Murray, B. Greig, A. Mesinger, J. B. Muñoz, Y. Qin, J. Park, and C. A. Watkinson, “21cmfast v3: A python-integrated c code for generating 3d realizations of the cosmic 21cm signal,” *arXiv preprint arXiv:2010.15121*, 2020.
- [3] X. Chen, “15 - mapping the universe with 21cm observations,” in *Big Data in Astronomy* (L. Kong, T. Huang, Y. Zhu, and S. Yu, eds.), pp. 379–406, Elsevier, 2020.
- [4] J. R. Pritchard and A. Loeb, “21 cm cosmology in the 21st century,” *Reports on Progress in Physics*, vol. 75, no. 8, p. 086901, 2012.
- [5] S. R. Furlanetto, S. P. Oh, and F. H. Briggs, “Cosmology at low frequencies: The 21 cm transition and the high-redshift universe,” *Physics reports*, vol. 433, no. 4-6, pp. 181–301, 2006.

-
- [6] K. M. Gerodias, “Simulations and data analysis for hirax and chord,” *McGill University*, 2023.
- [7] C. Evoli, A. Mesinger, and A. Ferrara, “Unveiling the nature of dark matter with high redshift 21 cm line experiments,” *Journal of Cosmology and Astroparticle Physics*, vol. 2014, no. 11, p. 024, 2014.
- [8] M. Valdes, A. Ferrara, M. Mapelli, and E. Ripamonti, “Constraining dark matter through 21-cm observations,” *Monthly Notices of the Royal Astronomical Society*, vol. 377, no. 1, pp. 245–252, 2007.
- [9] R. H. Brandenberger, R. J. Danos, O. F. Hernandez, and G. P. Holder, “The 21 cm signature of cosmic string wakes,” *Journal of Cosmology and Astroparticle Physics*, vol. 2010, no. 12, p. 028, 2010.
- [10] S. Balaji, M. E. Ramirez-Quezada, and C. Boehm, “Radio sky reveals primordial electron-proton interactions,” *arXiv preprint arXiv:2204.13711*, 2022.
- [11] P. K. Natwariya and A. C. Nayak, “Bounds on sterile neutrino lifetime and mixing angle with active neutrinos by global 21 cm signal,” *Physics Letters B*, vol. 827, p. 136955, 2022.

-
- [12] J. D. Bowman, A. E. Rogers, R. A. Monsalve, T. J. Mozdzen, and N. Mahesh, “An absorption profile centred at 78 megahertz in the sky-averaged spectrum,” *Nature*, vol. 555, no. 7694, pp. 67–70, 2018.
- [13] J. Mirocha, “Decoding the x-ray properties of pre-reionization era sources,” *Monthly Notices of the Royal Astronomical Society*, vol. 443, no. 2, pp. 1211–1223, 2014.
- [14] R. Barkana and A. Loeb, “In the beginning: the first sources of light and the reionization of the universe,” *Physics reports*, vol. 349, no. 2, pp. 125–238, 2001.
- [15] S. Wouthuysen, “On the excitation mechanism of the 21-cm (radio-frequency) interstellar hydrogen emission line,” *The Astronomical Journal*, vol. 57, pp. 31–32, 1952.
- [16] G. B. Field, “Excitation of the hydrogen 21-cm line,” *Proceedings of the IRE*, vol. 46, no. 1, pp. 240–250, 1958.
- [17] A. Liu, J. R. Pritchard, M. Tegmark, and A. Loeb, “Global 21 cm signal experiments: A designer’s guide,” *Physical Review D*, vol. 87, no. 4, p. 043002, 2013.
- [18] A. Cohen, A. Fialkov, R. Barkana, and R. A. Monsalve, “Emulating the global 21-cm signal from Cosmic Dawn and Reionization,” *Monthly Notices of the Royal Astronomical Society*, vol. 495, pp. 4845–4859, July 2020.

-
- [19] A. Mesinger, S. Furlanetto, and R. Cen, “21cmfast: a fast, seminumerical simulation of the high-redshift 21-cm signal,” *Monthly Notices of the Royal Astronomical Society*, vol. 411, no. 2, pp. 955–972, 2011.
- [20] J. Mirocha, S. R. Furlanetto, and G. Sun, “The global 21-cm signal in the context of the high- z galaxy luminosity function,” *Monthly Notices of the Royal Astronomical Society*, vol. 464, no. 2, pp. 1365–1379, 2017.
- [21] J. Mirocha, C. Mason, and D. P. Stark, “Effects of self-consistent rest-ultraviolet colours in semi-empirical galaxy formation models,” *Monthly Notices of the Royal Astronomical Society*, vol. 498, no. 2, pp. 2645–2661, 2020.
- [22] J. Mirocha, “Prospects for distinguishing galaxy evolution models with surveys at redshifts $z > 4$,” *Monthly Notices of the Royal Astronomical Society*, vol. 499, no. 3, pp. 4534–4544, 2020.
- [23] J. Mirocha, R. H. Mebane, S. R. Furlanetto, K. Singal, and D. Trinh, “Unique signatures of population iii stars in the global 21-cm signal,” *Monthly Notices of the Royal Astronomical Society*, vol. 478, no. 4, pp. 5591–5606, 2018.
- [24] J. Mirocha, S. Skory, J. O. Burns, and J. H. Wise, “Optimized multi-frequency spectra for applications in radiative feedback and cosmological reionization,” *The Astrophysical Journal*, vol. 756, no. 1, p. 94, 2012.

- [25] B. Zygelman, “Hyperfine level-changing collisions of hydrogen atoms and tomography of the dark age universe,” *The Astrophysical Journal*, vol. 622, no. 2, p. 1356, 2005.
- [26] L. Chuzhoy and P. R. Shapiro, “Ultraviolet pumping of hyperfine transitions in the light elements, with application to 21 cm hydrogen and 92 cm deuterium lines from the early universe,” *The Astrophysical Journal*, vol. 651, no. 1, p. 1, 2006.
- [27] C. M. Hirata, “Wouthuysen-field coupling strength and application to high-redshift 21-cm radiation,” *Monthly Notices of the Royal Astronomical Society*, vol. 367, no. 1, pp. 259–274, 2006.
- [28] S. Mittal and G. Kulkarni, “Ly α coupling and heating at cosmic dawn,” *Monthly Notices of the Royal Astronomical Society*, vol. 503, no. 3, pp. 4264–4275, 2021.
- [29] O. F. Hernández, “The global 21-cm signal of a network of cosmic string wakes,” *Monthly Notices of the Royal Astronomical Society*, vol. 508, no. 1, pp. 408–413, 2021.
- [30] O. F. Hernández, “Wouthuysen-field absorption trough in cosmic string wakes,” *Physical Review D*, vol. 90, no. 12, p. 123504, 2014.
- [31] J. O. Burns, S. Bale, N. Bassett, J. Bowman, R. Bradley, A. Fialkov, S. Furlanetto, M. Hecht, M. Klein-Wolt, C. Lonsdale, *et al.*, “Dark cosmology: Investigating dark matter & exotic physics in the dark ages using the redshifted 21-cm global spectrum,” *arXiv preprint arXiv:1902.06147*, 2019.

-
- [32] A. Schneider, “Constraining noncold dark matter models with the global 21-cm signal,” *Physical Review D*, vol. 98, no. 6, p. 063021, 2018.
- [33] K. K. Boddy, M. Lisanti, S. D. McDermott, N. L. Rodd, C. Weniger, Y. Ali-Haïmoud, M. Buschmann, I. Cholis, D. Croon, A. L. Erickcek, *et al.*, “Snowmass2021 theory frontier white paper: Astrophysical and cosmological probes of dark matter,” *Journal of High Energy Astrophysics*, vol. 35, pp. 112–138, 2022.
- [34] L. Philip, Z. Abdurashidova, H. Chiang, N. Ghazi, A. Gumba, H. Heilgendorff, J. Jáuregui-García, K. Malepe, C. Nunhokee, J. Peterson, *et al.*, “Probing radio intensity at high- z from marion: 2017 instrument,” *Journal of Astronomical Instrumentation*, vol. 8, no. 02, p. 1950004, 2019.
- [35] M. S. Rao, N. U. Shankar, R. Subrahmanyam, and S. Singh, “Detecting global signal from cosmic dawn and epoch of reionization with ska,” *Journal of Astrophysics and Astronomy*, vol. 44, no. 1, p. 24, 2023.